Effective Liquid Electrolytes for Enabling Room-Temperature Sodium–Sulfur Batteries

*Vittorio Marangon, Edoardo Barcaro, Francesco De Boni, Mirko Prato, Dominic Bresser, and Jusef Hassoun**

Glyme-based electrolytes for sodium-sulfur (Na–S) batteries are proposed for advanced cell configuration. Solutions of $NaClO_4$ or $NaCF_3SO_3$ in tetraglyme are investigated in terms of thermal stability, ionic conductivity, Na^+-transference number, electrochemical stability, stripping-deposition ability, and chemical stability in Na-cells. Subsequently, versions of the electrolytes doped with fluoroethylene carbonate (FEC) are prepared using 0.5, 1, 2, or 3% additive weight concentrations, and evaluated by adopting the same approach used for the bare solutions. Scanning electron microscopy (SEM) provides morphological details of the passivation layer formed on the Na electrodes, while X-ray photoelectron spectroscopy (XPS) sheds light on its composition. The most relevant achievement of the FEC-added electrolyte is the suppression of the polysulfide shuttle in Na–S cells using a cathode with 70 wt.% of sulfur in the composite. This result appears even more notable considering the low amount of the additive requested for enabling the reversible cell operation. The solutions using 1% of FEC show the best compromise between cell performance and stability. Cyclic voltammetry (CV) displays the potential region related to the FEC electrochemical process responsible for Na–S cell operation. The understanding of the electrolyte features enables additional cycling tests using sulfur cathode with an optimized current collector, increased specific capacity, and coulombic efficiency.

1. Introduction

Extensive research and development to allow the large-scale diffusion of electric or hybrid vehicles, as well as for massive exploitation of intermittent renewable energy sources, have been recently triggered by environmental schemes launched in several countries with the aim of mitigating concerns on climate change, possibly ascribed to human activities.[1] The lithium-ion battery (LIB) has been established as the technology of choice to fulfill the challenging requests of energy storage, due to the advantages of the Li-intercalation electrodes in terms of reversibility and specific energy density which exceeds 250 Wh kg^{-1}.[2–4] Despite the undeniable advantages, the materials used in LIB electrodes such as cobalt, nickel, manganese, copper, and lithium itself, are now posing serious concerns due to the expected decrease in availability and increase in cost.[5,6] In this complex scenario, sodium-based batteries are drawing increasing interest in view of the wide availability of the alkali metal and the remarkable energy content promoted by its low redox potential of −2.71 V versus SHE.[7–9] Among the various proposed sodium batteries, the Na–S one appeared the most appealing since it holds at the same time several bonuses, including the use of abundant, environmentally friendly, and low-cost materials, and the relevant theoretical energy density of the cell.[7] Indeed, the

V. Marangon, D. Bresser
Helmholtz Institute Ulm (HIU)
Helmholtzstrasse 11, 89081 Ulm, Germany
V. Marangon, D. Bresser
Karlsruhe Institute of Technology (KIT)
P.O. Box 3640, 76021 Karlsruhe, Germany
V. Marangon, E. Barcaro, J. Hassoun
Department of Chemical
Pharmaceutical and Agricultural Sciences
University of Ferrara
Via Fossato di Mortara 17, Ferrara 44121, Italy
E-mail: jusef.hassoun@unife.it, jusef.hassoun@iit.it
V. Marangon, J. Hassoun
Graphene Labs
Istituto Italiano di Tecnologia
Via Morego 30, Genoa 16163, Italy
F. De Boni, M. Prato
Materials Characterization Facility
Istituto Italiano di Tecnologia
Via Morego 30, Genoa 16163, Italy
J. Hassoun
National Interuniversity Consortium of Materials Science and Technology (INSTM)
University of Ferrara Research Unit
Via Mortara 17, Ferrara 44121, Italy

electrochemical conversion process between Na and S, summarized by the $16Na + S_8 \leftrightarrows 8Na_2S$ reaction, may lead to an energy density as high as 1274 Wh kg^{-1}.[10,11] Despite the notable expectation, the Na–S battery suffers from severe issues concerning the solubility of the high-order polysulfides such as Na_2S_8 and Na_2S_6 which can migrate by diffusion to the anode, reduce on its surface, and move back to the cathode to be newly oxidized within a shuttle process preventing the actual energy storage and shortening the cell life.[12,13] The remarkable insulant character of Na_2S alongside its detrimental deposition in the cell, and the relatively low reversibility of the charge-transfer process can further limit the possible application of this intriguing technology.[12,14] Great efforts to overcome these issues concerned all the cell components, including cathode,[15–19] anode,[20–22] interlayer,[12,23] and electrolyte,[24–29] with the aim of achieving a practical configuration of the Na–S battery. Nevertheless, the very limited benchmarking of the Na–S cell, and in particular of the electrolyte, hindered the actual evaluation of the various proposed breakthroughs. Recent reports have focused on the effects of the various solvents, conductive salts, and Na-protective additives on the Na/electrolyte interphase, however, only limited attention has been devoted to the influence of the single components and their concomitant effects on the electrochemical performance of the cell.[30–36] Indeed, further knowledge is still required to figure out the role of the sacrificial agent in allowing the use of the reactive metal anode in the Na–S battery. Beneficial effects on cell performance and efficiency have been attributed to the $NaNO_3$ additive, while a comprehensive study on its actual role is still needed.[37,38] Moreover, FEC has been proposed due to its passivation ability upon reduction with the alkali metals,[39,40] however with a focus on sodium-ion batteries (SIBs) rather than Na–S ones for which the appropriate concentration, reactivity, and role of this important sacrificial agent need considerable clarification. Therefore, we propose herein a step forward for the understanding of the role of the various electrolyte constituents on the Na–S electrode/electrolyte interphase in view of possible benchmarking. For this matter, tetraethylene glycol dimethyl ether (TEGDME) is hereafter selected as the favorite solvent to ensure suitable ions exchange and low flammability of the solutions,[41] and two common slats, i.e., $NaClO_4$ or $NaCF_3SO_3$, are chosen as the most adequate for electrolyte preparation. The electrochemical properties of the solutions are thoroughly studied to shed light on the differences deriving from the choice of the conductive salt, while the effect of the FEC addition is subsequently investigated. In particular, electrolytes containing either 0.5, 1, 2, or 3% in weight of FEC are screened in terms of physical-chemical and electrochemical features. Relevantly, a benchmark sulfur electrode exploiting 70 wt.% of active material in the composite is used to assess the electrochemical performance of the electrolytes in Na–S battery, and the most promising solutions are verified using an optimized, yet still scalable, sulfur electrode. The detailed study proposed in this work can allow the optimization of cells with reproducible outcomes beginning from the electrolyte, and therefore facilitate the achievement of advanced Na–S battery configurations characterized by potentially scalable performances.

2. Results and Discussion

The physical-chemical and electrochemical characteristics of the bare electrolytes intended as the ones dissolving either $NaClO_4$ (TE-Cl) or $NaCF_3SO_3$ (TE-F) without FEC addition are evaluated in **Figure 1** (all electrolytes acronyms and compositions are reported in **Table 1** for readers convenience). The TGA of the solutions performed under N_2 flow (Figure 1a) and the related differential (DTG) curves (Figure S1a in Supporting Information) display for both the electrolytes the main weight loss above 200 °C attributed to the TEGDME solvent evaporation, and an additional minor change at 245 °C likely due to the removal of crystallization solvent from salts complexes.[42–44] The salts degradation is observed at 530 °C for $NaClO_4$ in TE-Cl and 510 °C for $NaCF_3SO_3$ in TE-F (see TGA and DTG of solvents and salts in Figure S1b of Supporting Information). Moreover, TE-Cl shows a final weight variation from 780 °C possibly due to a further decomposition of $NaClO_4$ (Figure S1b of Supporting Information), while TE-F exhibits an additional loss at 290 °C, thus suggesting different solvent-salt complexes compared to TE-Cl. It is worth noting that the formation of such solvation complexes can influence the thermal trend of the $NaClO_4$ compared to the bare salt as evidenced by the TGA-DTG of Figure S1b (Supporting Information), which shows the increase of the degradation temperature from 530 to 560 °C, while $NaCF_3SO_3$ appears less influenced and shows approximately unaltered value (i.e., 510 °C). The ionic conductivity trends of TE-Cl and TE-F are investigated in the Arrhenius plots in Figure 1b. The values are obtained from the electrolyte resistance (R_e) at various temperatures determined by fitting the EIS Nyquist plots in Figure S2a,b (Supporting Information) through the non-linear least-square (NLLS) method (see Experimental section for details).[45,46] The two electrolytes show similar conductivity in the 10–74 °C interval, with values increasing from 6.1×10^{-4} to 1.7×10^{-3} S cm^{-1} for TE-Cl and from 5.2×10^{-4} to 1.2×10^{-3} S cm^{-1} for TE-F, although a notable difference is observed between 10 °C and −3 °C. Indeed, TE-Cl holds the quasi-linear variation with a remarkable final value of 5.0×10^{-4} S cm^{-1}, while TE-F conductivity abruptly decreases to 5.7×10^{-5} S cm^{-1}. This discrepancy is due to the efficient dissolution of $NaClO_4$ in TE-Cl even at lower temperatures, and the formation of lowly conductive crystalline phases including solvated $NaCF_3SO_3$ in TE-F at temperatures lower than 10 °C as suggested by the literature,[47] despite further effects ascribed to ion association with the formation of neutral couples without charge transport cannot be excluded.[37] On the other hand, both the solutions exhibit conductivity values suitable for battery application in the temperature range from 10 to 74 °C, while TE-Cl may be also suited for low-temperature operation. The ion mobility in TE-Cl and TE-F is further evaluated by determining the Na^+ transference number (t^+) at room temperature using the Bruce–Vincent–Evans method.[48] Accordingly, t^+ is calculated with Equation 1 (Experimental section) using the parameters in **Table 2** which are achieved by performing chronoamperometric tests on Na|Na cells and NLLS-fitting of the EIS Nyquist plots recorded before and after polarization (Figure S2c–f, Supporting Information).[45,46] Figure 1c reveals relatively high t^+ values for both solutions and suggests enhanced mobility of the

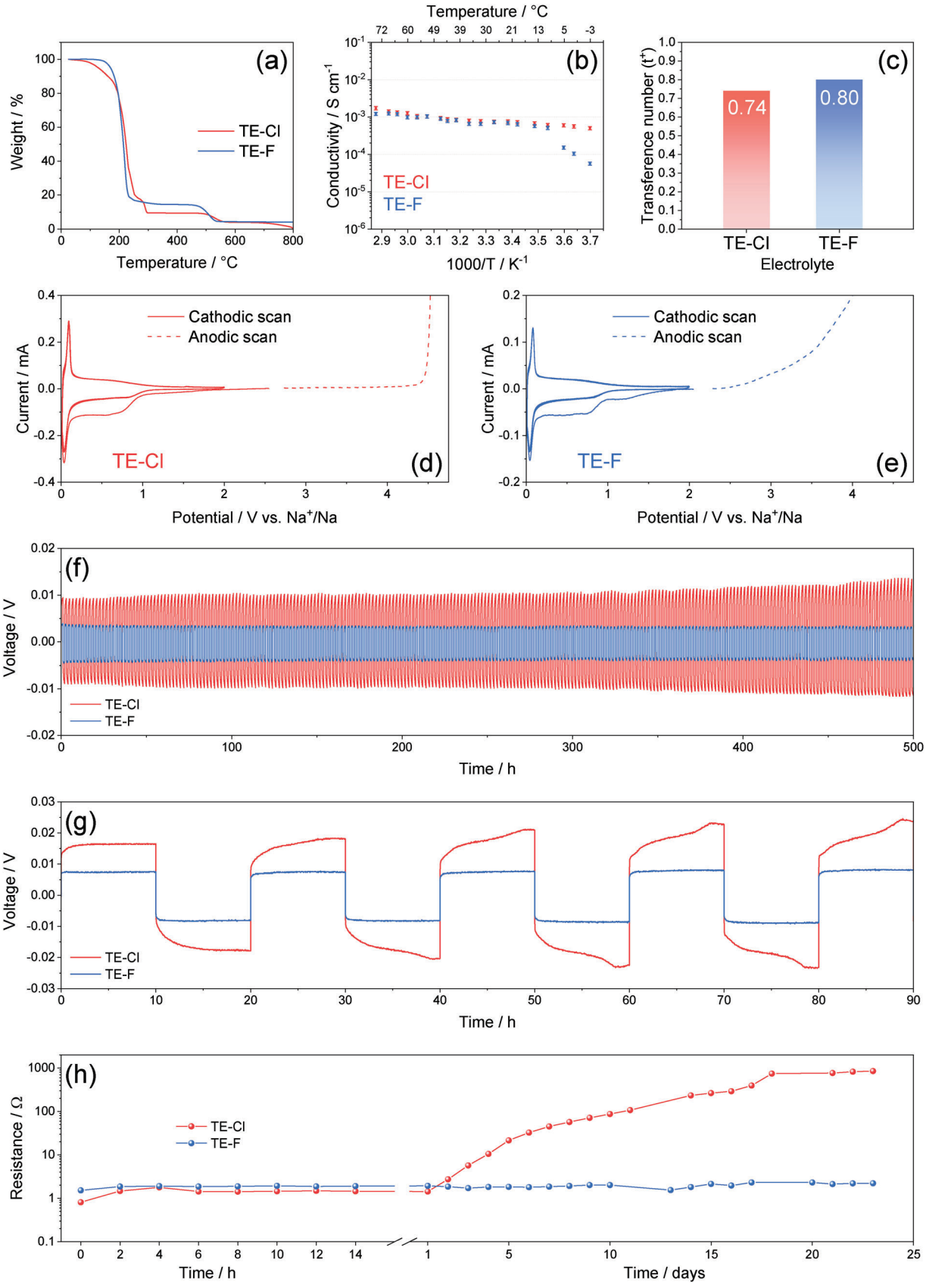
(a)
Weight / %
Temperature / °C
TE-Cl
TE-F
(b)
Temperature / °C
72 60 49 39 30 21 13 5 -3
Conductivity / S cm-1
1000/T / K-1
TE-Cl
TE-F
(c)
Transference number (t+)
0.74
0.80
TE-Cl
TE-F
Electrolyte
(d)
Current / mA
Cathodic scan
Anodic scan
TE-Cl
Potential / V vs. Na+/Na
(e)
Current / mA
Cathodic scan
Anodic scan
TE-F
Potential / V vs. Na+/Na
(f)
Voltage / V
TE-Cl
TE-F
Time / h
(g)
Voltage / V
TE-Cl
TE-F
Time / h
(h)
Resistance / Ω
TE-Cl
TE-F
Time / h
Time / days

Table 1. Acronyms and compositions of the investigated electrolytes.

Electrolyte acronym	Composition
TE-Cl	TEGDME, 1m $NaClO_4$
TE-Cl_0.5%	TEGDME, 1m $NaClO_4$ + 0.5% FEC
TE-Cl_1%	TEGDME, 1m $NaClO_4$ + 1% FEC
TE-Cl_2%	TEGDME, 1m $NaClO_4$ + 2% FEC
TE-Cl_3%	TEGDME, 1m $NaClO_4$ + 3% FEC
TE-F	TEGDME, 1m $NaCF_3SO_3$
TE-F_0.5%	TEGDME, 1m $NaCF_3SO_3$ + 0.5% FEC
TE-F_1%	TEGDME, 1m $NaCF_3SO_3$ + 1% FEC
TE-F_2%	TEGDME, 1m $NaCF_3SO_3$ + 2% FEC
TE-F_3%	TEGDME, 1m $NaCF_3SO_3$ + 3% FEC

Na^+ ions in line with the results achieved for similar glyme-based solutions,[24] despite the Bruce–Vincent–Evans method may lead to overestimated values in particular in the liquid electrolytes.[49] Furthermore, the lower t^+ value obtained for TE-Cl (0.74) compared with TE-F (0.80) indicates a faster ion mobility in the latter compared to the former, likely due to the different nature of the two salts. The electrochemical stability window (ESW) of TE-Cl and TE-F is determined with CV in the cathodic region (0.01–2.0 V versus Na^+/Na) and linear sweep voltammetry (LSW) in the anodic one (between OCV and 5.0 V versus Na^+/Na). Figure 1d,e shows the corresponding voltammograms revealing for both TE-Cl (Figure 1d) and TE-F (Figure 1e) a first reduction process at ≈0.7 V versus Na^+/Na, accounting for partial electrolyte reduction with the formation of a passivation layer or solid electrolyte interphase (SEI).[50] Reversible deposition/dissolution of Na ions between 0.05 and 0.08 V versus Na^+/Na and (de)insertion slightly below 1.0 V versus Na^+/Na can be also observed during the first cycle, as well as in the subsequent overlapping ones.[50] On the other hand, the two solutions show different anodic stability, which is taken as the potential value over which a non-negligible oxidation current of 30 μA is detected. Hence, TE-Cl exhibits electrolyte oxidation at 4.42 V versus Na^+/Na while TE-F shows the same behavior already at 2.98 V versus Na^+/Na. These values greatly influence the application range of the solutions since TE-Cl may be actually employed in Na batteries using phosphates- or layered oxide-based cathodes working above 3 V, while TE-F would be hardly suitable due to excessive side-reaction.[51–53] Nevertheless, the application in Na–S battery can be still considered both for TE-Cl and TE-F due to the operating voltage centered at ≈2.0 V of the electrochemical conversion process between Na and S.[21,24,54,55] With the aim of further testing the electrochemical stability, Figure 1f reports the sodium stripping/deposition tests carried out on Na|Na cells through galvanostatic cycling using a current of 0.1 mA cm^{-2}, and setting a step time of 1 h for charge and discharge. The results display the absence of sodium dendrites formation over 500 h of cycling and a low overvoltage, although significant differences between the solutions are observed. TE-Cl exhibits initial overvoltage of 9 mV which rapidly stabilizes at a steady state of 10 mV, and grows in the final stages to a maximum of 14 mV. Instead, TE-F shows a constant polarization slightly exceeding 3 mV for the whole testing time. These data are in line with the higher t^+ in TE-F than TE-Cl shown in Figure 1c, and further suggest a faster Na^+ transfer kinetics at room temperature leading to a lower polarization in the former compared to the latter. On the other hand, the increase of the overvoltage in TE-Cl at the end of the test can be ascribed to a slight growth of the passivation layer and the charge transfer resistance, possibly promoted by the relatively high density of $NaClO_4$ solution compared to other salts.[44,56] The stripping-deposition test in Figure 1g performed with a step time extended to 10 h evidences for TE-F a nearly constant square-shape overvoltage of 7 mV over 90 h of cycling, while an increasing slope is observed for TE-Cl with initial value of ≈17 mV growing to ≈25 mV at the end of the test. This behavior supports the formation of a thicker SEI layer on the Na electrodes which may increase the electrode/electrolyte interphase resistance when TE-Cl is employed rather than TE-F. Nevertheless, a more effective SEI is expected to efficiently protect the Na surface, in particular in view of possible application in Na–S cells. To shed light on this aspect, the variation of the electrode/electrolyte interphase resistance is analyzed in Figure 1h through EIS tests on Na|Na cells aged for 23 days using TE-Cl and TE-F, with values achieved by NLLS fitting of the Nyquist plots in Figures S3 and S4 (Supporting Information), and results listed in detail in Tables S1 and S2 (Supporting Information), respectively. The TE-Cl undergoes a relevant variation of the Nyquist plot shape (Figure S3, Supporting Information), and consequently of the number of elements accounting for the interphase (R_iQ_i) in the corresponding equivalent circuit, that is, from 1 with overall resistance of R_1 to 2 after 1 day with overall resistance of R_1+R_2, and back to 1 after 6 days, besides the element (R_wQ_w) accounting for the Warburg-type Na^+ diffusion (Table S1, Supporting Information). The continuous circuit modifications are concomitant with the notable increase of the electrode/electrolyte interphase resistance observed for TE-Cl, which raises from values between 1.0 and 1.5 Ω during the first 14 h upon cell assembly to almost 850 Ω after 23 days (Figure 1h) as the SEI grows and consolidates by aging.[57] On the other hand, the equivalent circuits associated with TE-F show variation limited to the diffusion elements, i.e., from (R_wQ_w) to Q_w (see Experimental section for details) while the interphase resistance holds a low and constant value of ≈2 Ω for the whole aging period (Figure 1h). Thus, the data confirm the consolidation of a highly resistive SEI on the Na electrodes using TE-Cl, while TE-F seems to be characterized by mild

Figure 1. Characterization of TE-Cl and TE-F: a) TGA performed under N_2 flow in the 25–800 °C temperature range, see DTG curves in Figure S1 of Supporting Information; b) Arrhenius plots reporting ionic conductivity trends determined by EIS at various temperatures, see related Nyquist plots in Figure S2 of Supporting Information; frequency range: 500 kHz–100 Hz; alternate voltage signal: 10 mV; c) histogram representation of the t^+ values calculated through Bruce–Vincent–Evans method (see equation 1 and Table 2),[48] see related chronoamperometric curves and Nyquist plots in Figure S2 of Supporting Information; (d, e) ESWs of d) TE-Cl and e) TE-F evaluated by CV (cathodic stability) in the 0.01–2.0 V versus Na^+/Na potential range and LSV (anodic stability) from the OCV condition to 5.0 V versus Na^+/Na; scan rate: 0.1 mV s^{-1}; (f, g) Na stripping/deposition tests achieved by applying a constant current rate of 0.1 mA cm^{-2} with step time of either f) 1 h or g) 10 h for charge and discharge; h) resistance trend versus time obtained through EIS carried out upon aging of Na|Na cells, see related Nyquist plots in Figures S3 and S4 and NLLS analyses in Tables S1 and S2 of Supporting Information; frequency range: 500 kHz–100 mHz; alternate voltage signal: 10 mV. See Table 1 for electrolyte acronyms.

Table 2. Parameters used in Equation 1 to calculate the t^+ values for TE-Cl and TE-F through the Bruce–Vincent–Evans method.[48] Current values are obtained by chronoamperometric curves displayed in Figure S2c,d of Supporting Information, while resistances are evaluated by applying the NLLS fitting method through the Boukamp software[45,46] on the Nyquist plots reported in Figure S2e,f of Supporting Information. See Table 1 for electrolyte acronyms.

Electrolyte	Initial current (I_0) [A]	Steady-state current (I_{ss}) [A]	Initial resistance (R_0) [Ω]	Steady-state resistance (R_{ss}) [Ω]	t^+
TE-Cl	1.26×10^{-3}	9.25×10^{-4}	0.52	0.81	0.74
TE-F	6.20×10^{-4}	5.00×10^{-4}	1.14	1.12	0.80

passivation. These outcomes evidence pronounced differences in the electrolyte properties depending on the use of either $NaClO_4$ or $NaCF_3SO_3$ conductive salt, not exclusively limited to the conductivity but also concerning the side reactions with Na.

The FEC-doped electrolytes are investigated by TGA performed in **Figure** 2a for the solutions using $NaClO_4$ (i.e., TE-Cl_0.5% - TE-Cl_3%) and in Figure 2b for the ones dissolving $NaCF_3SO_3$ (i.e., TE-F_0.5% - TE-F_3%), while the corresponding DTG curves are reported in Figure S5 (Supporting Information). The outcomes indicate for the TE-Cl family (Figure 2a) an initial weight loss beginning over 100 °C, with variations centered near 200 °C and between 220 and 240 °C. Despite the above weight losses being coherent with TEGDME and FEC evaporation (compare with Figure S1 in the Supporting Information), the solutions exhibit a complex response not linearly associated with the FEC content. This behavior might suggest the partial formation of a co-solvent between TEGDME and FEC, and the corresponding solvent-salt complexes, which would also explain the relevant weight loss in the FEC region at 200 °C, in contrast with the low additive amount ranging from 0.5 to 3%. Subsequently, the TE-Cl derivatives show weight losses at ≈280 °C due to the TEGDME-$NaClO_4$ crystallization solvent evaporation, and at 530 °C upon $NaClO_4$ degradation, in agreement with the TGA of TE-Cl discussed in Figure 1. On the other hand, the TGA curves of the FEC-doped TE-F (Figure 2b) display one main weight loss starting above 100 °C and centered at ≈200 °C due to the solvent and possible co-solvent removal, a barely detectable step over 250 °C related to solvent loss from TEGDME-$NaCF_3SO_3$ complexes, as well as a final one at 510 °C attributed to $NaCF_3SO_3$ degradation. Interestingly, the DTG curves in Figure S5 (Supporting Information) reveal for TE-F derivatives asymmetric peaks for the main loss at 200 °C, which may indicate additional contributes due to the presence of a co-solvent and related complexes. As already observed for TE-Cl family, the data suggest that low amounts of FEC can modify the thermal response and the solvation complexes also for the TE-F electrolytes which hold, at the same time, a suitable thermal stability. Na stripping/deposition measurements performed with a charge/discharge step time of 1 h are reported for the FEC-doped TE-Cl (Figure 2c) and TE-F (Figure 2d), alongside with the performance of bare solutions to facilitate the comparison. The data clearly indicate that the FEC remarkably raises the cell overvoltage due to the growth of a resistive SEI triggered by the additive reduction at the Na surface.[39] The figure also shows a notable change of the polarization during time, depending on the FEC amount and the employed conductive salt. In particular, the cell using TE-Cl_0.5% presents an initial polarization below 0.2 V which rapidly decreases after 100 h of cycling, and stabilizes below 0.1 V until the end of the test, while that employing TE-Cl_1% shows a similar behavior however with a slight polarization increase between 250 and 300 h of cycling to ≈0.2 V, and a rapid decrease after 300 h to a value of ≈0.03 V. Meanwhile, the cells with TE-Cl_2% and TE-Cl_3% maintain a constant overvoltage between 0.15 and 0.2 V over the whole test. The decrease of the Na|Na cell polarization can be related to a partial dissolution of the native SEI occurring during repeated cycling,[37] which is reasonably affected by the amount of FEC and possibly avoided with additive concentration ≥ 2% in the presence of $NaClO_4$. This behavior is expected to relevantly impact the Na cells' performance, since a partial dissolution of the native passivation layer may certainly lead to a less resistive electrode/electrolyte interphase, however it may provide a relatively weak protection of the Na surface. The cells using FEC-doped TE-F electrolytes exhibit a similar process, although the dissolution occurs earlier than the analog TE-Cl solutions (compare Figure 2d with Figure 2c), and can be avoided only by increasing the FEC content up to 3%. Indeed, the cell using TE-F_0.5% shows rapid decrease of the polarization from 0.16 to 0.05 V already after 30 h of cycling and a second gradual drop after 60 h leading to a minimum value of 0.013 V. On the other hand, the overvoltage of the cell with TE-F_1% gradually drops from 0.20 to 0.13 V during the initial 85 h, and then rapidly to 0.027 V until the end of the test, while the one with TE-F_2% passes from 0.23 to 0.18 V in 250 h, and then abruptly to a final value of 0.042 V. Instead, the cell using TE-F_3% displays a constant polarization between 0.15 and 0.20 V during the whole cycling test. Therefore, the partial dissolution of the SEI seems to have a different time-constant, depending either on the salt nature or on the FEC content. Nevertheless, the passivation of Na and its polarization is certainly increased by FEC, which promotes a further side process in addition to the one already observed for $NaClO_4$ and $NaCF_3SO_3$ with far lower overvoltage. Additional insight into the Na stripping/deposition is achieved by prolonging the charge/discharge time to 10 h in cells using FEC-doped TE-Cl (Figure 2e) and TE-F (Figure 2f). The cells using the TE-Cl family reveal a characteristic overvoltage evolving trough a reversible double wave with a slight stabilization after the first cycle, while a similar but less pronounced shape is observed for the ones using the TE-F family. The cell with TE-F_0.5% shows lower overvoltage compared to the one with TE-Cl_0.5%, and evolves according to a slowly polarized square signal already after 2 cycles. The cell using TE-F_1% appears similar yet more polarized than the one with TE-F_0.5%, and forms the square wave after 3 cycles, while the cells employing TE-F_2% and TE-F_3% maintain the double wave-shape during the whole cycling. These data confirm the relevant role of the FEC additive in promoting the formation of the passivation layer and influencing the Na extraction/deposition mechanism.

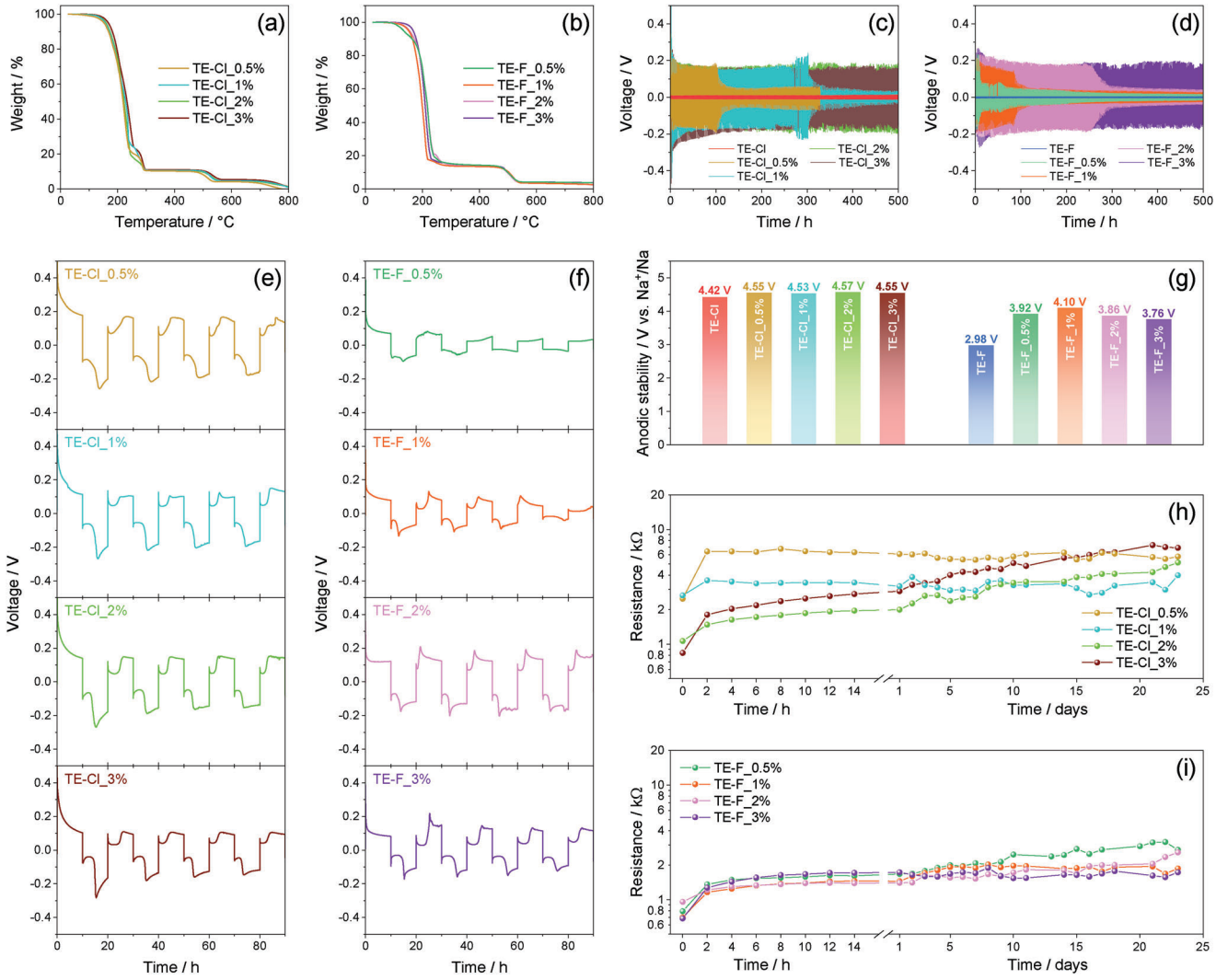

Figure 2. Characterization of the FEC-doped electrolytes (see Table 1 for compositions): a,b) TGA of the electrolytes dissolving either a) $NaClO_4$ or b) $NaCF_3SO_3$ performed under N_2 flow in the 25–800 °C temperature range, see related DTG curves in Figure S5 of Supporting Information; c–f) Na stripping/deposition tests achieved by applying a constant current of 0.1 mA cm^{-2} with step time of either c,d) 1 h or e,f) 10 h for charge and discharge on Na|Na cells using electrolytes dissolving (c, e) $NaClO_4$ or (d, f) $NaCF_3SO_3$; g) histogram representation of the anodic stability values measured by LSV, see Figure S6 and S7 in Supporting Information for voltammograms displaying the corresponding entire ESWs; scan rate: 0.1 mV s^{-1}; h,i) resistance trend versus time obtained through EIS carried out upon aging of Na|Na cells using electrolytes with h) $NaClO_4$ or i) $NaCF_3SO_3$, see related Nyquist plots in Figures S8 and S9, and NLLS analyses in Tables S3–S10 of Supporting Information; frequency range: 500 kHz–100 mHz; alternate voltage signal: 10 mV.

The latter aspect seems particularly pronounced when cells using the FEC-added solutions (Figure 2e,f) are compared with the bare electrolytes (Figure 1g) in which the exclusive contributes of the conductive salt and the solvent are expected.[58,59] In addition, the trends of Figure 2e,f indicate once more the higher solubility of the SEI formed at the Na surface in the TE-F solutions compared to TE-Cl ones, despite the presence of FEC. The ESW of the FEC-doped electrolytes is evaluated through CV in the cathodic region and LSV in the anodic one with voltammograms in Figures S6 and S7 (Supporting Information) for FEC-doped TE-Cl and TE-F, respectively. Figure 2g summarizes by histograms the related anodic stability (the values for TE-Cl and TE-F precursors are included for comparison). The TE-Cl solutions show during initial cathodic scan (Figure S6, Supporting Information) a first slight shoulder between 0.8 and 0.9 V versus Na^+/Na convoluted with the main reduction process at ≈0.5 V versus Na^+/Na, and a minor signal at 0.2 V versus Na^+/Na. The relative intensities of these cathodic peaks change with the variation of the FEC content, and appear associated with partial electrolyte reduction promoted by the additive, as indeed observed for carbonate-based solutions.[60] The subsequent voltammetry cycles evidence the reversible Na (de)insertion in the carbon at ≈0.6 V versus Na^+/Na, that occurs for all the electrolytes with remarkable stability.[50] Interestingly, only TE-Cl_0.5% clearly shows the reversible process between 0.01 and 0.10 V versus Na^+/Na ascribed to Na electrodeposition, which is apparently hindered by further increasing the additive content (Figure S6, Supporting Information). Very similar potential shapes, intensities, and variations are

displayed by the cells using TE-F-based electrolytes in the cathodic region (Figure S7, Supporting Information), with an additional minor signal during the first scan at 2.0 V versus Na^+/Na possibly due to specific side reactions of $NaCF_3SO_3$. Despite the similarities in the cathodic region, the FEC-added TE-Cl and TE-F electrolytes show relevant discrepancies of the anodic stability (Figure 2g). Hence, TE-Cl family stands up 4.5 V versus Na^+/Na, instead the TE-F one displays oxidation already between 3.8 and 4.1 V versus Na^+/Na. Furthermore, the data indicate that FEC addition slightly enhances the anodic stability of the TEGDME-$NaClO_4$ solution, and it strongly improves (≈1 V) the TEGDME-$NaCF_3SO_3$ one. This beneficial effect of FEC was recently observed for Li-based systems as well,[61] and it is likely due to the formation of a stable cathode electrolyte interphase (CEI) that protects the positive electrode and hinders the decomposition of the electrolyte at high voltages. Herein, the addition of FEC to the TEGDME-$NaCF_3SO_3$ electrolyte seemingly promotes an enhanced CEI compared to the exclusive use of the conducting salt, thanks to a synergy between $NaCF_3SO_3$ and the fluorinated carbonate that allows increased anodic stability. Figure 2h reports the interphase resistance trends of the FEC-doped TE-Cl solutions upon aging in Na|Na cells, with value obtained from the NLLS analyses of Tables S3–S6 (Supporting Information) performed on the EIS Nyquist plots displayed in Figure S8 (Supporting Information). The Nyquist plots can be represented with the $R_e(R_iQ_i)(R_wQ_w)$ equivalent circuit, except for TE-Cl_0.5% which modifies to $R_e(R_iQ_i)Q_w$ after cell assembly. The FEC-added electrolytes exhibit relevantly higher interphase resistance than the bare TE-Cl, with values at the OCV from 840 to 2600 Ω, sharply rising between 1500 and 6400 Ω already after 2 h of aging due to a relevant SEI growth.[57] Surprisingly, TE-Cl_0.5% presents the highest resistance (≈6000 Ω), and TE-Cl_1% displays remarkable values (from 3000 to 4000 Ω) from 2 h until the end of the test. Instead, TE-Cl_2% and TE-Cl_3% exhibit initial resistances of 1060 and 840 Ω, respectively, which progressively grow to 5100 and 6900 Ω in 23 days. These data suggest the fast formation of a resistive SEI in the solutions with lower FEC content (TE-Cl_0.5% and TE-Cl_1%), and a slowed down growth of the film in those with higher additive amount (TE-Cl_2% and TE-Cl_3%). Moreover, TE-Cl_1% reveals after 23 days the lowest interphase resistance (≈ 4000 Ω) with the most stable trend, suggesting a suitable compromise for Na-cell application. Except for the initial 2 h of test, the TE-F electrolytes added by FEC show a rather different behavior than TF-Cl ones, as demonstrated by the trends of the interphase resistance in Figure 2i which is based on the NLLS analyses reported in Tables S7–S10 (Supporting Information) of the Nyquist plots in Figure S9 (Supporting Information). The same $R_e(R_iQ_i)(R_wQ_w)$ equivalent circuit represents all cells, while the analysis reveals a fast initial resistance increase from 690–960 to1160–1360 Ω, accounting for the relevant reduction of the electrolytes occurring in 2 h, and the subsequent progressive raise leading to values between 1700 and 2700 Ω. It is worth mentioning that the highest resistance is achieved after 23 days in the cell using TE-F_0.5%, whilst the lowest value is related to the one using TE-F_3%.

Figure 3 reports a detailed investigation carried out by FTIR spectroscopy on the electrolytes to provide further insights into their composition, as well as by ex situ SEM performed on Na electrodes aged in contact with the TEGDME-based solutions for 1 month (see the Experimental section) to observe the morphological features of the SEI in dependence of the electrolyte composition. As deduced from the FTIR spectra in Figure 3a, both the TEGDME-$NaCF_3SO_3$-based and the TEGDME-$NaClO_4$-based electrolyte solutions reveal the expected combination of signatures due to the solvent and the respective conducting salt. Indeed, $NaCF_3SO_3$ is identified by signals at 638 and 1033 cm^{-1} corresponding to the symmetric SO_3 vibration and stretching, respectively, as well as by peaks at 755 and 1225 cm^{-1} related to the CF_3 band stretching,[62] while the $NaClO_4$ contribution is revealed by the vibrational mode of ClO_4^- at 624 cm^{-1}.[63] On the other hand, the FEC is observed by signals with intensity increasing in concomitance to its concentration in the solutions, that is, at 727 and 767 cm^{-1} due to the O—C—O ring breathing mode,[61] at 1647 cm^{-1}, which is usually observed for CF-containing species,[64] and at 1833 cm^{-1}, identifying the C═O vibrational mode.[65] Interestingly, a minor peak is observed at 1722 cm^{-1}, with a detectable intensity only for TE-F_2%, TE-Cl_0.5%, and TE-Cl_3%, which may be attributed to carbonate species deriving from FEC side reactions within the solutions.[66,67] The effects of the composition of the solutions on the properties of the passivation film on the Na electrode are investigated by SEM in Figure 3b–u. The sodium sample treated with TE-Cl (Figure 3b,c) presents an irregular surface characterized by indented micrometric agglomerates across the electrode surface, indicating a poor passivation ability of the bare combination of the TEGDME solvent and the $NaClO_4$ conducting salt. Remarkably, the addition of a limited amount of FEC in TE-Cl_0.5% is sufficient to form a thin SEI layer on Na, despite the presence of multiple cracks and nanometric agglomerates on the surface observed in the corresponding micrographs (Figure 3d,e). Following this trend, the treatment with TE-Cl_1% leads to an SEI with a characteristic morphology, where the homogeneous layer shows porous regions approaching sizes of ≈10 μm (Figure 3f,g). The further increase of the FEC concentration in TE-Cl_2% and TE-Cl_3% thickens the SEI layer, leading to the formation of submicrometric clusters scattered around the electrode surface for the former (Figure 3h,i), and to the complete coverage of Na for the latter (Figure 3j,k), likely suggesting an excessive electrode passivation. The sodium samples aged in contact with the TEGDME-$NaCF_3SO_3$-based solutions display a similar growth trend as for the previous ones, however with a considerably different morphology of the corresponding SEIs. Indeed, TE-F leads to an irregular disposition on the Na surface of spherical aggregates with sizes of <1 μm (Figure 3l,m), while Na passivation is observed upon aging with TE-F_0.5% where the SEI displays deep cracks until the metal surface (Figure 3n,o). The increase of the FEC content in TE-F_1% causes a uniform coverage of the Na surface through an SEI with heterogeneous morphology (Figure 3p,q), which undergoes an abrupt thickening and partial cracking when the FEC content is further increased in TE-F_2% (Figure 3r,s). This trend is consistent with the SEM data acquired for TE-F_3%, where the further thickening of the passivation film leads to the formation of submicrometric crystal-like structures scattered around the electrode surface (Figure 3t,u). Notably, the SEM analyses reported in Figure 3 indicate the relevant or likely excessive Na passivation upon contact with solutions having FEC concentration ≥2%, as indeed hypothesized in the discussion of Figure 2. On the other hand, the mild passivation promoted by

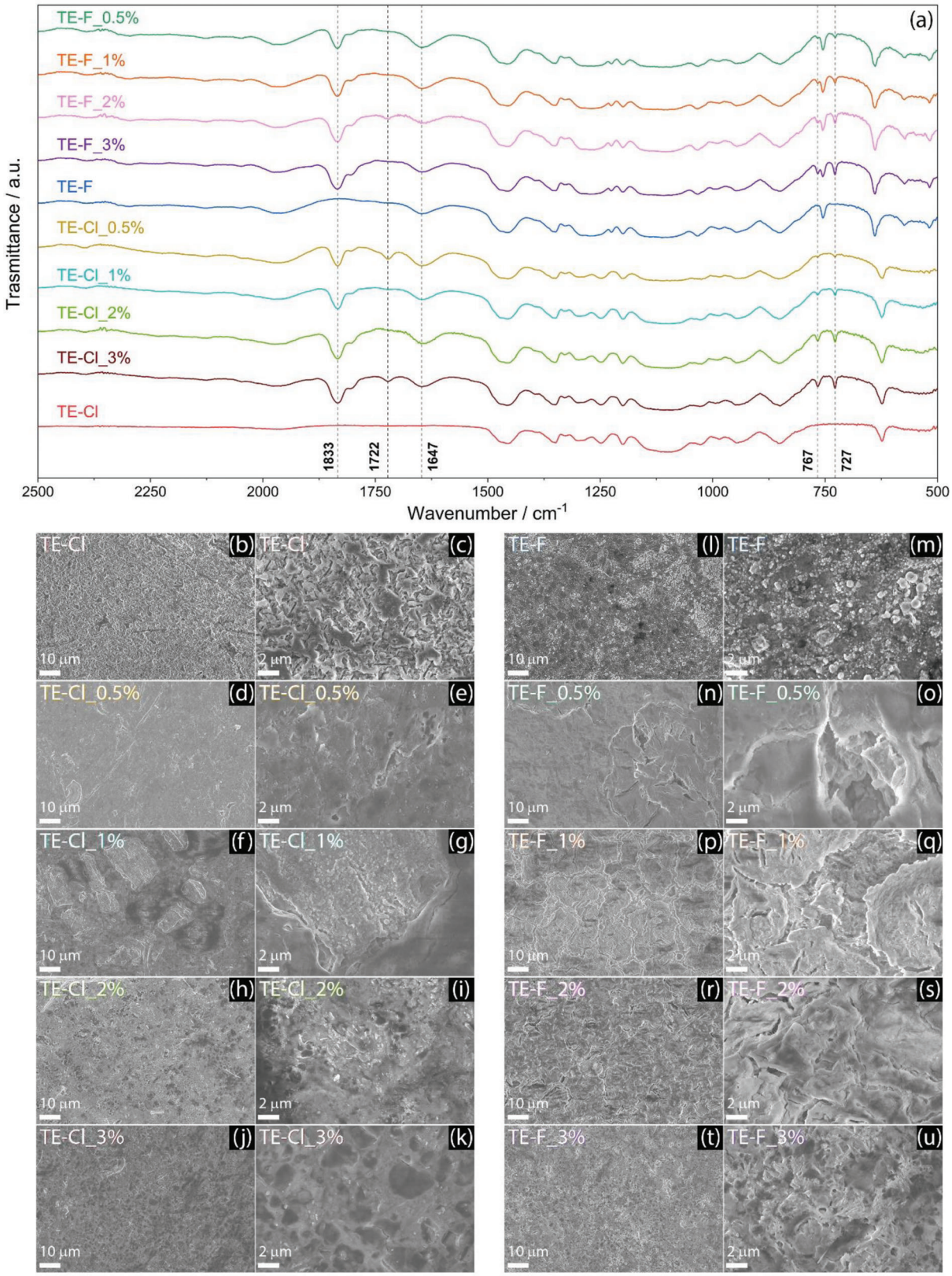

Figure 3. a) FTIR spectra of the TEGDME-based electrolytes; b–u) SEM images at various magnifications of Na electrodes aged in contact with b,c) TE-Cl, d,e) TE-Cl_0.5%, f, g) TE-Cl_1%, h,i) TE-Cl_2%, j,k) TE-Cl_3%, l,m) TE-F, n,o) TE-F_0.5%, p,q) TE-F_1%, r,s) TE-F_2% and t,u) TE-F_3% in Na|Na cells. See Table 1 for electrolyte acronyms.

the solutions with FEC concentration of either 0.5% or 1% can facilitate the Na^+ ions diffusion toward the sodium electrode, while excessive passivation is expected to prevent an adequate operation of the metallic anode and depress the Na–S cell response.

The composition of the passivation film formed on the Na surface in the bare electrolytes and the ones modified with FEC addition is investigated through XPS in **Figure 4**. The Na samples are retrieved from Na|Na cells aged for more than 20 days with either TE-Cl, TE-F, TE-Cl_3%, or TE-F_3% (see Experimental section for details). The survey spectra related to TE-Cl and TE-F in Figure 4a share the Na, C, and O signals, and also reveal the expected differences due to $NaClO_4$ and $NaCF_3SO_3$ reduction products, respectively. TE-Cl exhibits signals in Cl 2p regions,[68] while peaks in the F 1s, F KLL, and S 2p peaks are detected for TE-F.[69,70] Some detail on the SEI composition is obtained from the corresponding high-resolution spectra reported in Figure 4b–j. The Na 1s signal ascribed to the formation of NaCl and NaF precipitates at the Na surface as well as due to the metal itself appears at (1071.5 ± 0.2) eV for both TE-Cl (Figure 4b) and TE-F (Figure 4f).[31] In addition, contributes of the C—C, C—O, and C═O bonds due to the reduction of the TEGDME solvent to carbonates and organic species are deducted from the C 1s signals at (284.8 ± 0.2), (286.3 ± 0.2) and (287.5 ± 0.2) eV for TE-Cl (Figure 4c) and TE-F (Figure 4g).[31] Further contributes at (289.0 ± 0.2) and (293.9 ± 0.2) eV ascribed to O—C═O and C-F bonds, respectively, are observed only for TE-F (Figure 4g) as indeed expected from the fluorinated salt.[70] Interestingly, the O—C═O signal suggests in TE-F the formation of a characteristic SEI with a significant amount of organic fraction upon glyme reduction in the presence of $NaCF_3SO_3$.[70] The O 1s region shows for TE-Cl (Figure 4d) and TE-F (Figure 4h) composite peaks, that are deconvoluted into the Na KLL Auger peak at ≈536 eV, the contribution at ≈531 eV accounting for Na—O interactions in sodium-ethers, oligomers, carbonates, and oxides,[31,70] and another peak between 532 and 533 eV confirming the presence of C—O bonds[31] as well as Cl—O ones.[71] The Cl 2p signals for TE-Cl (Figure 4e) consist of two $2p_{3/2}/2p_{1/2}$ doublets at 208.5/210.1 and 206.3/207.9 eV of ClO_4 and ClO_3 groups, respectively, due to the salt deposition and reduction at the Na-interphase.[68,72] On the other hand, TE-F displays the typical signals in the F 1s (Figure 4i) and S 2p (Figure 4j) regions due to C—F (688.6 ± 0.2 eV), Na—F (683.8 ± 0.2 eV) and S—O ($2p_{3/2}/2p_{1/2}$ doublet at 169.2/170.4 eV) interactions deriving from $NaCF_3SO_3$ decomposition.[73,74] The role of FEC on the SEI composition is evaluated in Figure 4k, which reports the survey spectra of Na samples from sodium symmetrical cells using TE-Cl_3% and TE-F_3%. As expected, TE-Cl_3% reveals the presence of weak F KLL and F 1s signals ascribed to FEC, and a slight decrease of the Cl 2p wave intensity. The corresponding high-resolution spectra in Figure S10a,b (Supporting Information) confirm the C-F and Na-F interactions in the F 1s interval, as well as the retained ClO_4 and ClO_3 doublets in the Cl 2p range. These modifications well suggest a partial covering by the FEC decomposition products of the SEI deriving from glyme solvent and salt. A similar influence of FEC is observed for TE-F_3%, since a modification in the shape of the F 1s peak and the almost suppression of the S 2p signal can be observed in Figure S10c,d (Supporting Information), respectively. Therefore, the XPS data reveal the concomitant contributes of the TEGDME solvent, the salts (i.e., either $NaClO_4$ and $NaCF_3SO_3$), and the FEC additive to the by-products forming the passivation layer covering the Na surface. These products lead to unique SEI compositions, with atomic percentages extracted from the XPS and reported in **Table 3**. The SEI layers deriving from TE-F and TE-F_3% show almost the same composition in terms of Na, C, O, and F, with the exception of S which greatly decreases from 3.1% in TE-F to 1.7% in TE-F_3%. On the other hand, a decrease of Na, C, and Cl, a great increase of O, alongside the presence of F can be observed by comparing TE-Cl and TE-Cl_3%, thus suggesting the preferential formation in the outer layers of inorganic species, such as sodium carbonates and chlorates. The XPS outcomes appear in line with the different properties observed in Na-Na symmetrical cells, and evidence a relevant dependence of the SEI composition on the electrolyte formulation which is expected to affect the electrochemical performance of Na–S cells.

The two electrolyte sets are hereafter tested in Na–S cells at the constant current rate of C/20 (1C = 1675 mA g^{-1}) between 1.4 and 2.6 V as reported in Figures 5 (TE-Cl set) and 6 (TE-F set) using a sulfur-Super P carbon black (S:SPC) 70:30 *w/w* cathodic composite cast on bare aluminum (see Experimental section for details). **Figure 5a** shows the voltage-time profile during the first cycle of Na–S cells using the TE-Cl set, and indicates remarkable differences promoted by the FEC addition to the electrolyte. Hence, the voltage of the cell using the bare TE-Cl shows two discharge plateaus at 2.25 and 1.72 V with slopes accounting respectively for the formation of high-order polysulfides Na_2S_x ($4 \leq x \leq 8$) and short-order ones ($2 \leq x \leq 4$) upon conversion reaction between Na and S.[12,14] Subsequently, two charge steps at 1.95 and 2.32 V upon oxidation of the polysulfides are observed,[12,14] the latter of which proceeds without any end until the time cut-off of 20 h adopted as protection (see Experimental section). This behavior clearly indicates a severe polysulfide shuttle process, which is typically promoted by a poorly protected Na surface, favoring a continuous reaction of the soluble Na_2S_x species with the metal anode.[75] On the other hand, the shuttle reaction is somehow mitigated in the second cycle (Figure 5b) and progressively vanishes upon several cycles (see 30^{th} cycle in Figure 5c). The addition of FEC even at very low concentration almost fully hinders the shuttle reaction, and remarkably allows the completion of the charging process already at the first cycle, as shown in Figure 5a for the cells using TE-Cl_0.5%, TE-Cl_1%, TE-Cl_2% and TE-Cl_3%. Furthermore, the curves related to the first cycle show the occurrence of an additional discharge plateau at ≈1.95 V, the magnitude of which increases by raising the FEC content due to the electrochemical reduction of the additive already observed through CV in the cathodic region (Figures S6 and S7 in Supporting Information). It is worth mentioning that the shape of the charge profile of the Na–S cell may also reflect a contribution of the FEC to the plateaus related to the oxidation of the polysulfides, thus possibly suggesting a role of the additive on the kinetics of the Na–S process. The second cycle (Figure 5b) evidences for the FEC-doped solutions a well-defined multi-step discharge/charge process, the shape of which depends on the additive content, while the TE-Cl precursor shows partial deactivation of the high-voltage discharge step. After 30 cycles (Figure 5c), the Na–S conversion process is almost fully hindered in the cells using TE-Cl_2% and TE-Cl_3%, instead, the ones using TE-Cl_0.5% and TE-Cl_1% still reveal

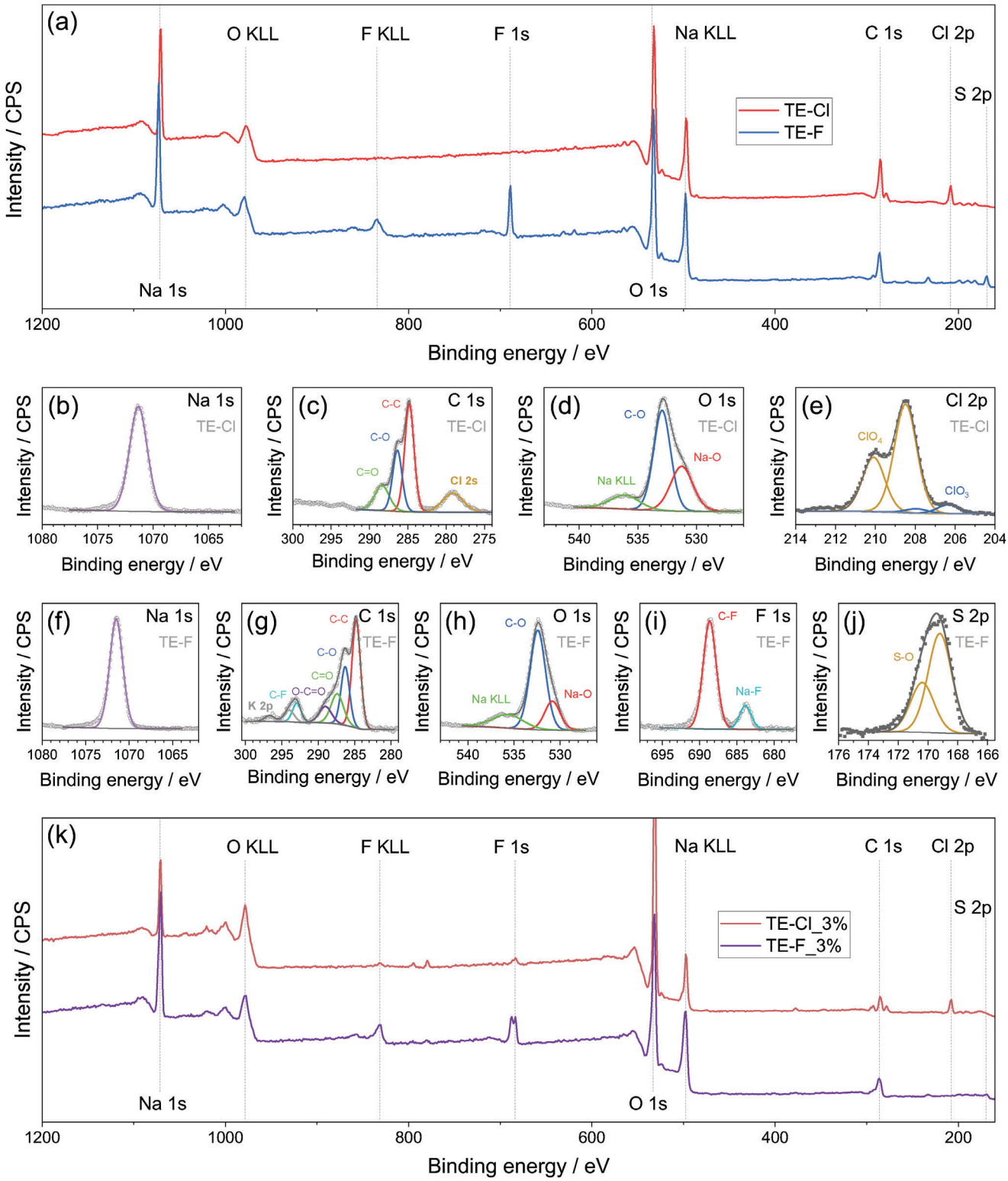

Figure 4. XPS analyses of sodium electrodes retrieved from Na|Na cells using TE-Cl, TE-F, TE-Cl_3% or TE-F_3%. In detail: a) survey spectra related to TE-Cl and TE-F; b–e) high-resolution spectra recorded in b) Na 1s, c) C 1s, d) O 1s and e) Cl 2p regions for TE-Cl; f–j) high-resolution spectra recorded in f) Na 1s, g) C 1s, h) O 1s, i) F 1s and j) S 2p regions for TE-F; k) survey spectra related to TE-Cl_3% and TE-F_3%. See Table 1 for electrolyte acronyms.

Table 3. Atomic percent compositions recorded through XPS on the surface of Na samples collected from Na-cells using either TE-Cl, TE-F, TE-Cl_3% or TE-F_3%. See Figure 4 for related XPS spectra, the Experimental section for sodium treatment, and Table 1 for electrolyte acronyms.

Electrolyte	Na [%]	C [%]	O [%]	Cl [%]	F [%]	S [%]
TE-Cl	11.2	41.5	41.6	5.7	0	0
TE-F	14.8	31.0	40.5	0	10.6	3.1
TE-Cl_3%	7.4	15.2	71.4	3.9	2.1	0
TE-F_3%	15.2	30.3	41.9	0	10.8	1.7

a reversible reaction with acceptable magnitude. These results, in combination with the features of the electrolytes in Na-metal cells discussed in Figures 2 and 3, indicate that the excessive SEI growth and consequent resistance increase for TE-Cl_2% and TE-Cl_3% may limit the evolution of the Na–S electrochemical process. Figure 5d shows the discharge capacity and coulombic efficiency trends over cycling for the various Na–S cells discussed above. The cell using TE-Cl exhibits an initial capacity slightly below 400 mAh g^{-1}, that subsequently decreases to 200 and reaches ≈130 mAh g^{-1} at the steady state, with very modest values of the coulombic efficiency (40–60%) and final failure possibly due to dendrites formation. The low efficiency is clearly ascribed to the above-discussed shuttle process affecting the cell with the bare electrolyte (see top-side panels a, b, c in Figure 5), which finally leads to irregularities of the SEI promoting in principle the metal dendrites on the Na surface.[12,13] On the other hand, the addition of FEC is reflected in the increase of the first cycle capacity to ≈700, 800, 900, and 1000 mAh g^{-1} for the cells with TE-Cl_0.5%, TE-Cl_1%, TE-Cl_2%, and TE-Cl_3%, respectively. This initial capacity increase is due to the contribution of the FEC redox reaction, which progressively vanishes during the subsequent cycles. Besides the side action of the additive, the Na–S cells using the

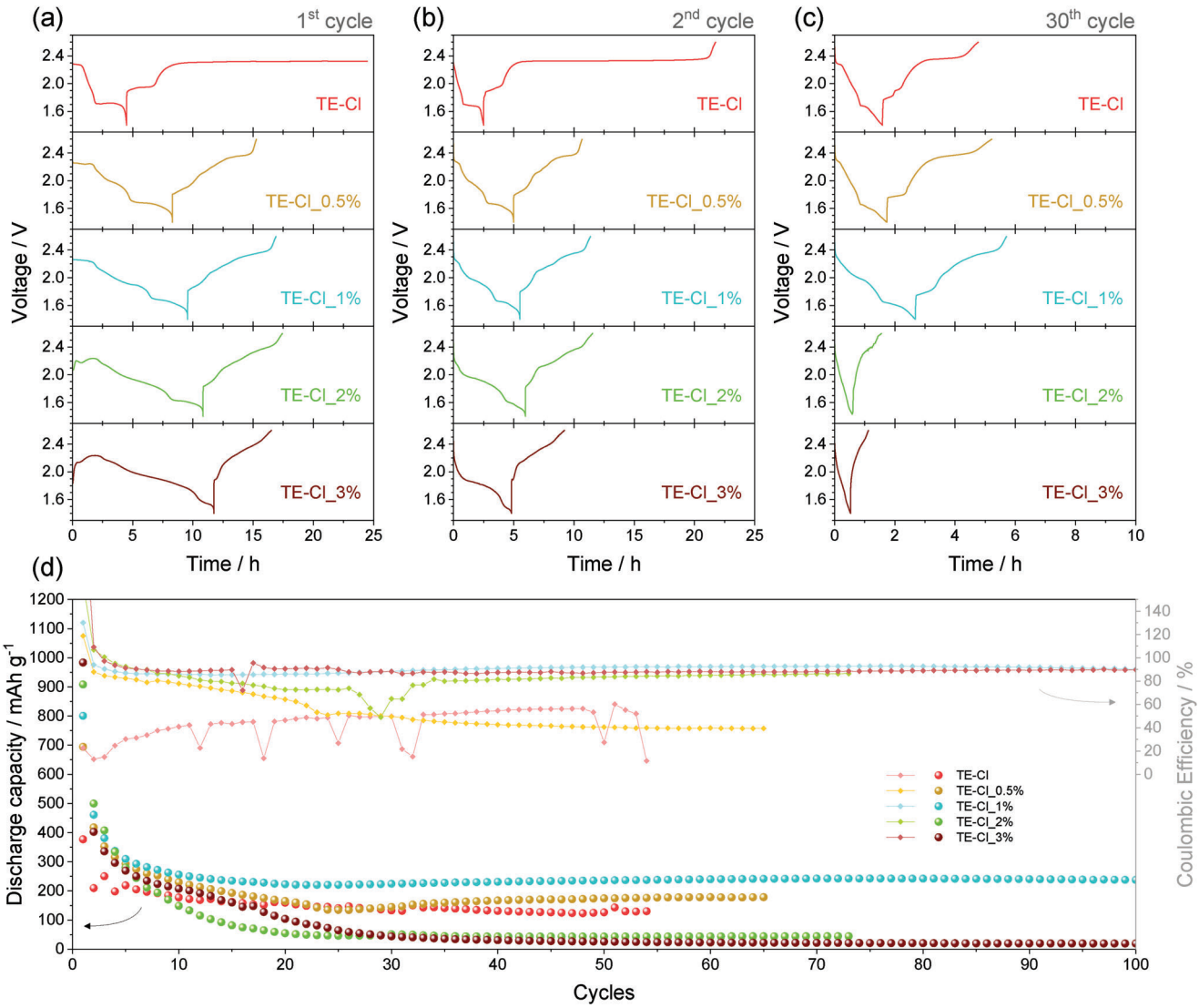

Figure 5. Galvanostatic cycling tests performed on Na–S cells using electrolytes dissolving $NaClO_4$ (see Table 1 for compositions): a–c) voltage profiles versus time of the a) 1st, b) 2nd, and c) 30th cycle, and d) corresponding capacity trends versus cycle number with right *y*-axis reporting coulombic efficiency; constant current rate: C/20 (1C = 1675 mA g_S^{-1}); voltage range: 1.4–2.6 V; electrode: S:SPC 70:30 *w/w* on Al support.

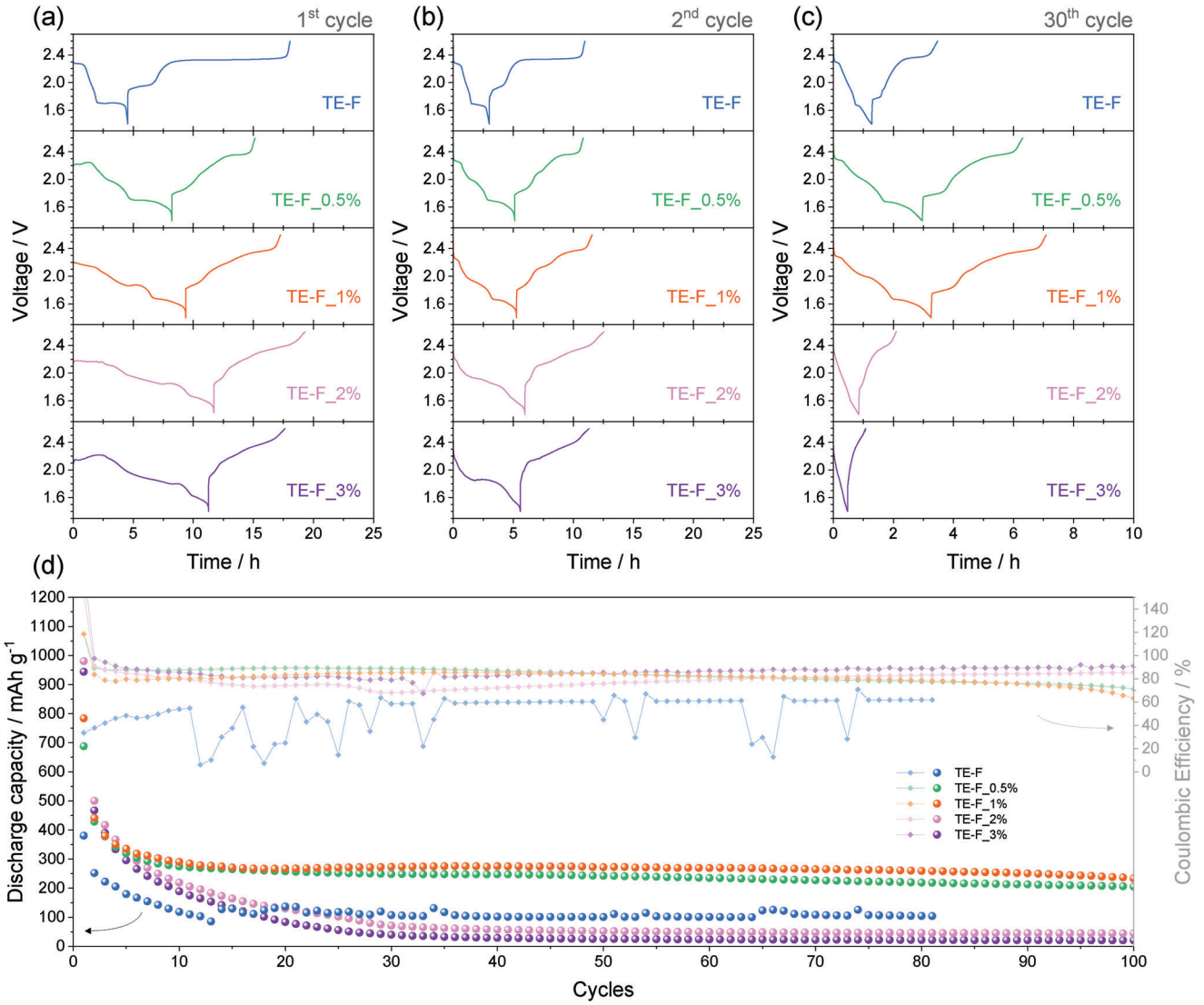

Figure 6. Galvanostatic cycling tests performed on Na–S cells using electrolytes dissolving $NaCF_3SO_3$ (see Table 1 for compositions): a–c) voltage profiles versus time of the a) 1st, b) 2nd, and c) 30th cycle, and d) corresponding capacity trend versus cycle number with right *y*-axis reporting coulombic efficiency; constant current rate: C/20 (1C = 1675 mA g_S^{-1}); voltage range: 1.4–2.6 V; electrode: S:SPC 70:30 *w*/*w* on Al support.

doped electrolytes reveal a remarkable increase of the coulombic efficiency to values approaching 90% as the shuttle process is mitigated. The cells using TE-Cl_0.5% and TE-Cl_1% reveal suitable capacity trends with steady-state values of 180 and 240 mAh g^{-1}, respectively, despite only the latter exhibiting cycle life over 100 cycles, notable retention (238 mAh g^{-1} at the end of the test), and constant coulombic efficiency exceeding 90%. Instead, the cells using TE-Cl_2% and TE-Cl_3% show a fast drop of the discharge capacity to 40 mAh g^{-1} only after 30 cycles, despite a coulombic efficiency approaching 90%. These discrepancies may be ascribed to a less effective SEI in TE-Cl_0.5%, an excessive film growth in TE-Cl_2% and TE-Cl_3%, and possibly to an optimal condition in TE-Cl_1%. Hence, a relevant growth of the passivation layer using TE-Cl_2% and TE-Cl_3% can certainly prevent the dendrites formation, however, it may strongly increase the interphase resistance and limit the Na–S conversion process. Instead, an insufficient protection of Na due to the relatively low FEC content in TE-Cl_0.5% can promote partial polysulfide shuttle, thus decreasing the cell efficiency, leading to the loss of active material and lowering the Na–S cell capacity.

The Na–S cells using TE-F-based solutions show in **Figure 6** analog performances to those with TE-Cl-based electrolytes discussed in Figure 5. The cell using bare TE-F exhibits at the first cycle (Figure 6a top panel) the two plateaus during discharge attributed to the formation of sodium polysulfides, reversed into a double-step charge due to their electrochemical oxidation with a prolonged high-voltage plateau ascribed to the polysulfides shuttle, however less extended than the one observed for the bare TE-Cl (compare with Figure 5a, top panel).[12,14] The latter process is in part limited during subsequent cycles upon the consolidation of the SEI (Figure 6b,c). The addition of FEC leads to the expected mitigation of the shuttle process and the concomitant

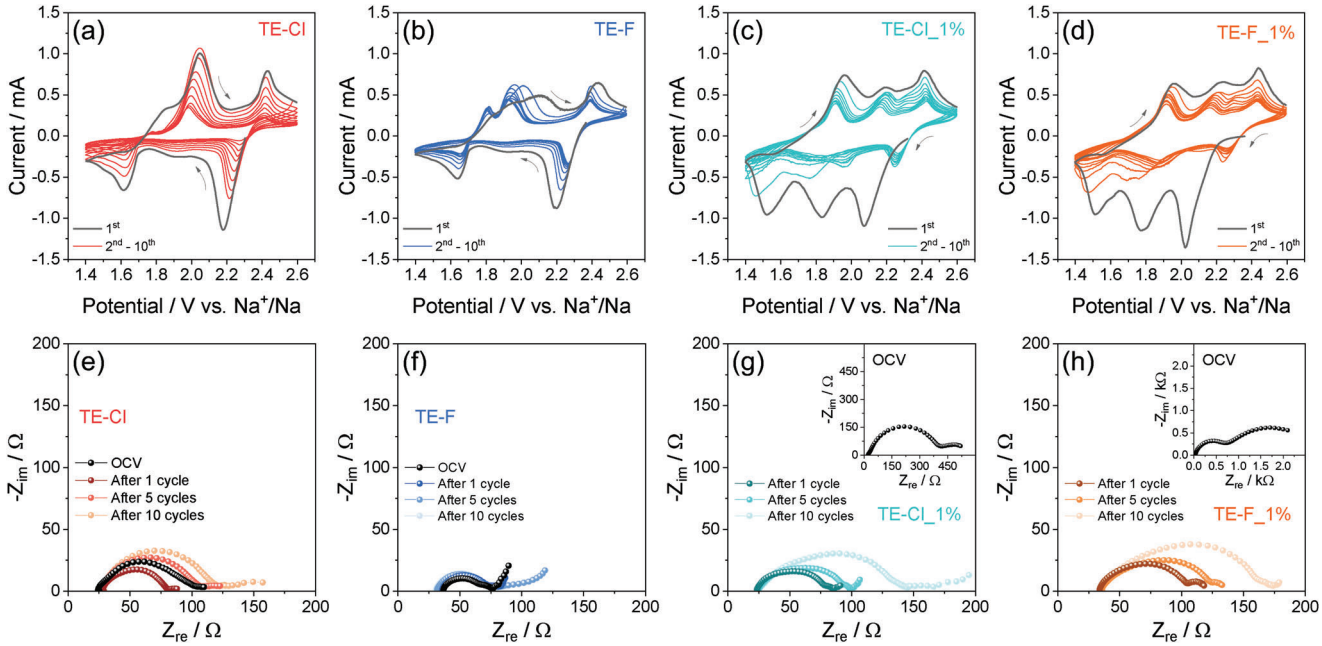

Figure 7. a–d) CV measurements and e–h) EIS tests carried out on Na–S cells using either a,e) TE-Cl, b,f) TE-F, c,g) TE-Cl_1%, d,h) TE-F_1% electrolytes. EIS spectra recorded at the cell OCV condition and after 1, 5, and 10 cycles. CV potential range: 1.4–2.6 V versus Na^+/Na; scan rate: 0.1 mV s^{-1}; EIS frequency range: 500 kHz–100 mHz; alternate voltage signal: 10 mV. See Table 1 for electrolyte acronyms.

appearance of new redox steps both in charge and in discharge (Figure 6a), with magnitude raising from TE-F_0.5% to TE-F_1% and TE-F_2%, despite TE-F_2% and TE-F_3% show similar first discharge. The voltage profiles during the subsequent cycles (Figure 6b,c) show for cells using TE-F_2% and TE-F_3% the progressive deactivation of the Na–S conversion due to excessive passivation of Na (see Figure 3), while TE-F_0.5% and TE-F_1% lead to a well reversible evolution of the discharge/charge Na–S plateaus. Similarly to TE-Cl solutions, Figure 6d shows low efficiency and failure due to dendrite growth for the cell using bare TE-F electrolyte, with the most enhanced cycling behavior, efficiency, and capacity retention for the TE-F_0.5% and TE-F_1%, and a fast capacity decay despite the high efficiency for TE-F_2% and TE-F_3%. Also in the case of TE-F electrolyte, the addition of the FEC promotes the first cycle capacity from 400 mAh g^{-1} (TE-F) to a maximum approaching 1000 mAh g^{-1} (TE-F_2% and TE-F_3%). Furthermore, the cell using bare TE-F reveals a steady-state capacity of ≈100 mAh g^{-1} with occasional drops due to dendrites, and a columbic efficiency as low as ≈60% as the shuttle process runs, thus confirming the poor characteristics of the SEI. Meanwhile, the cells using TE-F_2% and TE-F_3% exhibit efficiency increased between 80 and 90%, however with rapid capacity decrease suggesting the hindering of the reaction between Na and S due to a sluggish electrode/electrolyte interphase. Relevantly, TE-F_0.5% and TE-F_1% show cycle life extended over 100 cycles, with steady-state capacity of 220 and 260 mAh g^{-1}, respectively, and coulombic efficiency exceeding 80%. It is worth mentioning that the efficiency of the latter cells decreases to values between 60 and 70% at the end of the test possibly due to a partial dissolution of the SEI at the Na surface. Hence, the cell using TE-F_0.5% (Figure 6d) reveals a longer cycle life with respect to the one using TE-Cl_0.5% (Figure 5d), thus suggesting a more stable interphase in the former than in the latter, which is possibly promoted by an optimized interplay between the FEC additive and $NaCF_3SO_3$ salt compared to $NaClO_4$ one in this specific concentration. On the other hand, the slightly enhanced capacity of TE-F_1% (Figure 6d) with respect to TE-Cl_1% (Figure 5d) associated with a lower coulombic efficiency indicates for the Na–S cell using the former electrolyte a less resistive but more soluble SEI, in line with the electrolytes' properties studied in Figures 1 and 2. Therefore, the data recorded in Figures 5 and 6 indicate the addition of 1% of FEC to the TE-Cl and TE-F as the most suitable condition to achieve, at the same time, long cycle life, enhanced capacity, and acceptable coulombic efficiency of the Na–S cell.

To further investigate the modification of the electrode/electrolyte interphase during Na–S cycling and the influence of the FEC on the reaction kinetics, CV measurements coupled with EIS are performed in Na–S cells using the TE-Cl and TE-F electrolyte precursors as well as the most performing FEC-added solutions according to Figures 5 and 6, that is, TE-Cl_1% and TE-F_1%. **Figure 7** reports the voltammograms recorded between 1.4 and 2.6 V versus Na^+/Na (Figure 7a–d) and the Nyquist plots at the OCV condition of the cells and after 1, 5, and 10 cycles (Figure 7e–h). The cell using bare TE-Cl shows at the first cycle (Figure 7a) two main reduction signals at 2.2 and 1.6 V versus Na^+/Na in line with galvanostatic profiles in Figure 5, attributed to polysulfides formation including an intermediate shoulder at ≈1.9 V versus Na^+/Na during the conversion from Na and S to Na_2S_x.[12,24] The subsequent oxidation evidences a double-peak extending from 1.7 to 2.2 V versus Na^+/Na, and a second signal centered at ≈2.4 V versus Na^+/Na in accordance with the conversion of the polysulfide intermediates back to Na and S.[12,21] It is worth mentioning that the polysulfide shuttle observed for the cells using the bare

Table 4. NLLS analyses carried out on the Nyquist plots reported in Figure 7, recorded upon CV of Na–S cells using either the TE-Cl, TE-F, TE-Cl_1%, or TE-F_1% electrolyte. The NLLS method is applied through the Boukamp software by exclusively accepting fits with a χ^2 value of the order of 10^{-4} or lower.[45,46] See Table 1 for electrolyte acronyms.

Electrolyte	Cell condition	Circuit	R_1 [Ω]	R_2 [Ω]	R_3 [Ω]	R_i ($\sum R_n$) [Ω]	χ^2
TE-Cl	OCV	$R_e(R_1Q_1)(R_2Q_2)(R_wQ_w)$	5.19 ± 5.09	73.6 ± 2.0	/	78.7 ± 3.9	2×10^{-4}
	1 CV cycle	$R_e(R_1Q_1)(R_wQ_w)$	53.5 ± 0.3	/	/	53.5 ± 0.3	6×10^{-5}
	5 CV cycles	$R_e(R_1Q_1)(R_wQ_w)$	76.2 ± 1.2	/	/	76.2 ± 1.2	8×10^{-5}
	10 CV cycles	$R_e(R_1Q_1)(R_wQ_w)$	78.4 ± 0.7	/	/	78.4 ± 0.7	1×10^{-5}
TE-F	OCV	$R_e(R_1Q_1)(R_2Q_2)Q_w$	30.4 ± 2.5	9.02 ± 2.9	/	39.4 ± 2.7	3×10^{-4}
	1 CV cycle	$R_e(R_1Q_1)(R_2Q_2)Q_w$	34.1 ± 1.2	16.6 ± 2.2	/	50.7 ± 1.8	3×10^{-5}
	5 CV cycles	$R_e(R_1Q_1)(R_2Q_2)Q_w$	38.6 ± 3.6	19.5 ± 2.9	/	58.1 ± 3.3	4×10^{-5}
	10 CV cycles	$R_e(R_1Q_1)(R_2Q_2)Q_w$	38.5 ± 1.0	13.5 ± 1.5	/	52.0 ± 1.3	2×10^{-5}
TE-Cl_1%	OCV	$R_e(R_1Q_1)(R_2Q_2)(R_wQ_w)$	10.2 ± 0.7	343 ± 2	/	353 ± 2	3×10^{-5}
	1 CV cycle	$R_e(R_1Q_1)(R_2Q_2)Q_w$	12.6 ± 3.0	36.8 ± 3.4	/	49.4 ± 3.2	4×10^{-5}
	5 CV cycles	$R_e(R_1Q_1)(R_2Q_2)Q_w$	35.7 ± 5.5	25.1 ± 4.9	/	60.8 ± 5.2	1×10^{-4}
	10 CV cycles	$R_e(R_1Q_1)(R_wQ_w)$	112 ± 4	/	/	112 ± 4	8×10^{-4}
TE-F_1%	OCV	$R_e(R_1Q_1)(R_wQ_w)$	599 ± 6	/	/	599 ± 6	2×10^{-5}
	1 CV cycle	$R_e(R_1Q_1)(R_2Q_2)$	74.8 ± 0.7	13.9 ± 1.2	/	88.7 ± 1.0	9×10^{-5}
	5 CV cycles	$R_e(R_1Q_1)(R_2Q_2)(R_3Q_3)$	33.6 ± 4.0	56.9 ± 4.4	10.6 ± 1.1	101 ± 4	1×10^{-5}
	10 CV cycles	$R_e(R_1Q_1)(R_2Q_2)(R_3Q_3)$	37.6 ± 8.6	91.6 ± 9.9	10.4 ± 2.9	140 ± 8	6×10^{-5}

solution during charge in the galvanostatic cycling in Figure 5 is not clearly detected during oxidation in the CV of Figure 7a, mostly due to the difference between the two techniques which can influence the occurrence of this process. Indeed, CV is based on a potential scan during which the current can notably rise in correspondence to the occurrence of the Na–S electrochemical process, instead the galvanostatic cycling proceeds at a constant and relatively low current that may allow a relevant shuttle reaction. The second cycle reveals some change in the CV shape and peak position, associated with morphological rearrangement of the sulfur cathode and SEI formation, which typically modify the electrode conductivity and the cell polarization as observed in previous work.[76] More relevantly, Figure 7a depicts for the cell using the bare TE-Cl an abrupt decrease of peak intensity upon the subsequent cycles, a relevant deactivation of the charge peaks at 2.0 and 2.4 V versus Na^+/Na, and the discharge ones at 2.2 and 1.7 V versus Na^+/Na, as well as an additional slight shoulder detected as a weak signal at ≈1.75 V versus Na^+/Na during charge. This behavior may be attributed to the rapid loss of the active material, i.e., sulfur, caused by the polysulfide reaction and deposition at the anode side which is particularly effective in the presence of a weak SEI layer.[76,77] The voltammograms of TE-F (Figure 7b) show at the first cycle the same processes already observed for TE-Cl, however with hindered kinetics suggested from the broad peak during first oxidation between 1.7 and 2.2 V versus Na^+/Na. The above wave is deconvoluted into a defined double peak centered at 1.8 and 1.9 V versus Na^+/Na during subsequent cycles, with profile change and potential shifts induced by the already mentioned electrode morphological changes.[76] Furthermore, Figure 7b displays a mitigated deactivation of the Na–S conversion in TE-F compared to TE-Cl (Figure 7a), thus suggesting a better interphase formed in the TEGDME-$NaCF_3SO_3$ electrolyte rather than the equivalent one using $NaClO_4$, despite the galvanostatic tests in Figures 5 and 6 demonstrated the failure of both systems upon prolonged cycling in Na–S cell. The cells using TE-Cl_1% (Figure 7c) and TE-F_1% (Figure 7d) reveal an electrochemical process strongly influenced by the FEC addition. Hence, the systems exhibit three peaks during the first discharge at 2.0, 1.8, and 1.5 V versus Na^+/Na rather than the two observed in the bare solution, reflected in corresponding charge signals at 2.0, 2.2, and 2.4 V versus Na^+/Na. The presence of an additional reversible peak at 1.8 V versus Na^+/Na during discharge well agrees with the cycling data discussed previously and confirms the effective reduction of the FEC occurring in the Li-S battery concomitantly with the electrochemical conversion reaction. Moreover, the activation, stabilization, and definition of the peaks during the subsequent cycles suggest the effective role of the additive in stabilizing a characteristic Li-S redox process which differs from the one observed without FEC, both in terms of peak position and shape (compare panels c and d with a and b in Figure 7). The mitigated deactivation of the CV response observed for the FEC-added solutions reflects the enhancement of the electrode/electrolyte interphase already discussed in the galvanostatic cycles of Figures 5 and 6. On the other hand, the CV tests show a progressive weakening and potential shift toward lower potential values of the discharge process at 1.5 V versus Na^+/Na, thus suggesting that the reduction of the long-chain polysulfides to short-chain ones occurring at low potential becomes incomplete and affected by a polarization increase with the ongoing of the cycles. The Nyquist plots recorded upon voltammetry of Figure 7e–h are analyzed through NLLS method using equivalent circuits including various elemens as previously discussed, with outcomes collected in **Table 4** to shed light on the electrode/electrolyte interphase behavior during Na–S conversion reaction.[45,46] The cell using TE-Cl (Figure 7e) exhibits an initial resistance of ≈79 Ω that decreases to 54 Ω after the first cycle in line with the activation of the interphase,[76]

and increases to 78 Ω at the end of the test, thus accounting for a gradual growth of the SEI film.[31] On the other hand, TE-F (Figure 7f) shows a low R_i with slight increase from 39 to 51 Ω after one cycle, and stabilization between 50 and 60 Ω during the subsequent ones in line with the better CV results (Figure 7b) compared to TE-Cl (Figure 7a). A different scenario is presented by TE-Cl_1% (Figure 7g) and TE-F_1% (Figure 7h), which reveal the expected interphase activation after one cycle with drastic decrease of R_i from 353 and 599 to 49 and 89 Ω, respectively. Subsequently, the data indicate a progressive resistance increase to reach at the end of the tests 112 Ω for TE-Cl_1% and 140 Ω for TE-F_1%, likely due to the Na/electrolyte interphase features already discussed in Figure 2h,i, with an additional contribute of the sodium polysulfides to the SEI growth.[78] Moreover, the lower final resistances deriving from the $NaClO_4$-FEC system are in line with a more stable interphase with respect to $NaCF_3SO_3$-FEC, as already suggested by the cycling performance in Figures 5 and 6. Therefore, the CV and EIS data confirm the relevant influence of FEC not only on SEI characteristics but also on the features of the Na–S conversion process.

The deactivation of the discharge process at 1.5 V versus Na^+/Na upon cycling observed above may be associated with the features of the electrochemical reduction process to short-chain polysulfides. With the aim of investigating a deeper conversion degree, additional CV and galvanostatic measurements are performed in Na–S cells by lowering the reduction limit from 1.4 V down to 1.0 V and using a sulfur cathode with an improved few-layer graphene (FLG)-coated aluminum current collector rather than the bare metallic foil used in the previous experiments (see Experimental section). **Figure 8** shows in panels a and b the voltammograms recorded with the enlarged potential limits for the Na–S cells using TE-Cl_1% and TE-F_1%, respectively. The CV profiles show for both the systems the Na–S conversion signals already observed in Figure 7, including the stabilization and definition of the peaks during subsequent cycles and the completion of the low voltage discharge process at 1.5 V versus Na^+/Na due to the lower potential cut-off. In agreement with CV of Figure 7, a substantial decrease of peak intensity during reduction is detected between 1st and 2nd cycle, in line with active material loss particularly promoted in this case by the adopted low cut-off voltage that leads to irreversible formation of short-chain sodium polysulfides, and possibly to side electrolyte reduction.[76,77] In addition, after a few CV cycles the two cells reveal in Figure 8a,b an unexpected failure possibly induced by the lowered discharge cut-off. A similar scenario is evidenced by the galvanostatic cycling tests within the extended limits in Figure 8c,d, which display respectively the voltage profiles at C/20 between 1.0 and 2.6 V related to TE-Cl_1% and TE-F_1%. After a few cycles during which the Na–S conversion occurs properly, a sudden noise appears during charge and leads to fast failure of the cells analogously to CV. A possible explanation for this phenomenon may be found in the excessive precipitation of low-chain polysulfides such as Na_2S_2 or Na_2S formed below 1.4 V,[26] and their reactivity with amorphous and high surface area carbon, such as the carbon black (super P) used in the electrode formulation (see Experimental Section). The above-mentioned reactivity of Na_2S with carbon, also documented by the safety data sheets of commercial products and literature,[79] can lead to gas evolution possibly affecting the cathode mechanical stability and leading to cell failure, such as that observed in Figure 8a–d. Moreover, the reaction between sulfides and the FEC carbonyl group cannot be excluded, as suggested by the modification of the Na–S responses promoted by the presence of the additive observed previously. To verify in part this hypothesis, and exclude a possible role of the FLG-coated aluminum support, new Na-S cells are cycled at C/20 between limits restricted again to 1.4–2.6 V, and compared with those employing the bare aluminum already reported in Figures 5 and 6. The voltage profiles of the cells using TE-Cl_1% (Figure 8e) and TE-F_1% (Figure 8g) with the optimized sulfur cathode show the typical evolution of the Na–S conversion process, with the irreversible capacity promoted by the FEC reaction at the first cycle,[80] and the stable and reversible multi-step discharge/charge processes occurring through the subsequent cycles. Relevantly, the cycling trends for TE-Cl_1% (Figure 8f) and TE-F_1% (Figure 8h) display a slight enhancement in performance with respect to the systems using the benchmark sulfur cathode coated on bare aluminum, both in terms of delivered capacity and coulombic efficiency. The FLG-coated support allows a steady state cell capacity after 50 cycles of 282 mAh g^{-1} in TE-Cl_1% with respect to the 236 mAh g^{-1} of the bare aluminum, and final value of 270 mAh g^{-1} instead of 237 mAh g^{-1} (Figure 8f). Moreover, the cell using the optimized electrode delivers a coulombic efficiency exceeding 97% during the whole test, instead of values between 90 and 92% associated with the benchmark electrode (Figure 8f). Meanwhile, the cell using TE-F_1% with the FLG-coated support shows a steady state capacity after 50 cycles of 307 mAh g^{-1} and a final value of 287 mAh g^{-1}, instead of 272 and 233 mAh g^{-1}, respectively, shown for the cells using the bare Al (Figure 8h). Improved coulombic efficiency is also demonstrated by the cells using the optimized sulfur electrode compared to the benchmark in TE-F_1%, with values of 90% after 50 cycles and 88% at the end of the test rather than 84% and 63%, respectively. More importantly, these measurements suggest that the increase back of the discharge cut-off from 1.0 to 1.4 V can actually avoid the cell failure and drawbacks observed in the tests of Figure 8a–d, and almost completely exclude possible detrimental effects on the cell performance of the FLG-coated current collector, which instead enhances the performance in terms of delivered capacity and efficiency.[81] In this regard, panels a-c of Figure S11 (Supporting Information) report photographic images of electrodes and separator retrieved after a few cycles at C/20 in the 1.0–2.6 V voltage range in TE-Cl_1% (i.e., after the test reported in Figure 8c), while panels d-f of the same figure display the respective cell components after 100 cycles between 1.4 and 2.6 V with the same electrolyte (i.e., after the test shown in Figure 8e). The photographs evidence for the components cycled between 1.0 and 2.6 V (Figure S11a–c, Supporting Information) irregular swellings on the cathode surface and mark-up (Figure S11a, Supporting Information) likely promoted by mechanical stress due to gas evolution, bubbling, or volume change. Furthermore, the almost uniform dark color of the separator may account on the cathode side for the short-chain polysulfides formation (Figure S11b, Supporting Information, left panel) and on the anode side for Na dendritic structure infiltration (Figure S11b, Supporting Information, right panel). Moreover, the metallic anode surface presents a dark and rough surface suggesting substantial polysulfide precipitation at the SEI (Figure S11c, Supporting Information). The cell components

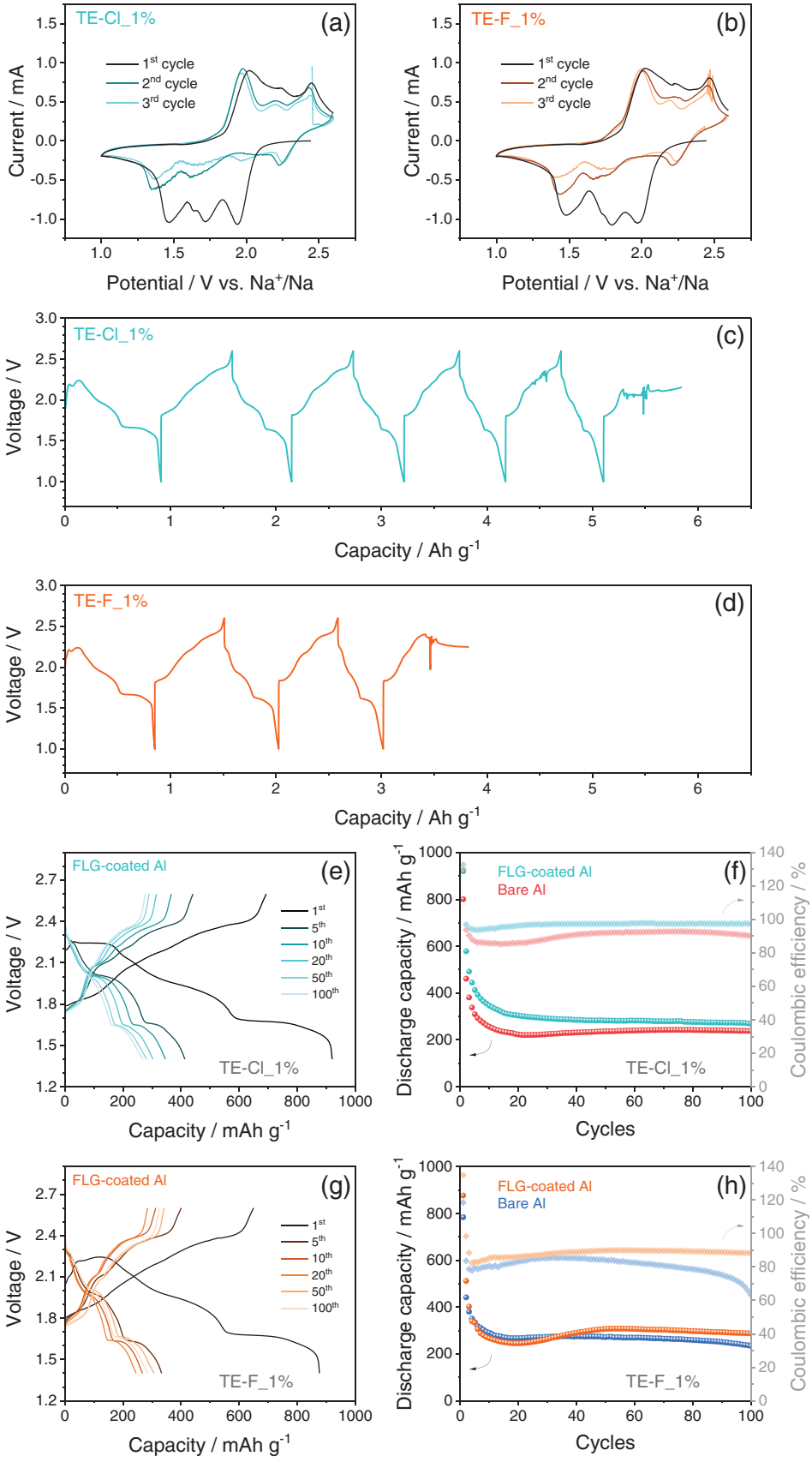
TE-Cl_1%
(a)
1st cycle
2nd cycle
3rd cycle
Current / mA
Potential / V vs. Na+/Na
TE-F_1%
(b)
1st cycle
2nd cycle
3rd cycle
Current / mA
Potential / V vs. Na+/Na
TE-Cl_1%
(c)
Voltage / V
Capacity / Ah g-1
TE-F_1%
(d)
Voltage / V
Capacity / Ah g-1
FLG-coated Al
(e)
1st
5th
10th
20th
50th
100th
TE-Cl_1%
Voltage / V
Capacity / mAh g-1
FLG-coated Al
Bare Al
(f)
TE-Cl_1%
Discharge capacity / mAh g-1
Coulombic efficiency / %
Cycles
FLG-coated Al
(g)
1st
5th
10th
20th
50th
100th
TE-F_1%
Voltage / V
Capacity / mAh g-1
FLG-coated Al
Bare Al
(h)
TE-F_1%
Discharge capacity / mAh g-1
Coulombic efficiency / %
Cycles

cycled between 1.4 and 2.6 V (Figure S11d–f, Supporting Information) exhibit instead a more regular surface of the sulfur cathode compared to the previous one, with traces of passivation precipitates expected upon long cycling (Figure S11d, Supporting Information). The separator at the cathode side (Figure S11e, Supporting Information, left panel) depicts in this cell a lighter color compared to the one of the cell cycle within the extended voltage limits, while the opposite face likely reveals the absence of Na dendrites (Figure S11e, Supporting Information, right panel). The sodium side of this latter cell shows a smoother passivated surface than the previous one, which is notably achieved over a long charge/discharge galvanostatic test (Figure S11f, Supporting Information). It is also worth mentioning that the dark residues on the anode surfaces due to separator detachment upon opening are much more evident in the cell tested within the extended voltage cut-off (panel c) than in the one using the restricted voltage range (panel f). Therefore, the data provided in Figure 8 and Figure S11 (Supporting Information) indicate the crucial role of the cathode composition and operational voltage limits to ensure reversible and safe Na–S cycling at room-temperature. In addition, the outcomes of Figures 5 and 6 highlight the importance of the electrolyte features for allowing Na–S application, and demonstrate that even limited modifications in the solution composition may actually drive the successful cell operation and avoid its failure. The effective approach we propose can also shed light on the critical role of the additive used to enhance the Na–S performance which, on the other hand, influences the Na–S conversion steps leading to new processes that still require investigation.[26,28,82] Further improvement may be indeed achieved by setting up the proper electrolyte design before focusing on the cathode architecture to get higher capacity in Na–S batteries.[83,84] The results achieved herein are compared with the recent literature in Table S11 in the Supporting Information in terms of active material content in the cathode composite, the charge/discharge cut-off voltages, and the steady state capacity, that is, the most stable value provided by the cell. The comparison is carried out by taking into consideration a similar sulfur loading (1–2 mg cm^{-2}) and comparable discharge–charge rates. The outcomes clearly show that higher capacity values can be delivered by Na–S cells, although by using a considerably wider charge/discharge voltage window and a lower sulfur content in the cathode composite. Indeed, various works reported sulfur composites with an S content ranging from <30 wt.%[85] to 40–50 wt.%,[23,86–94] while only a few of them investigated mixtures with an S content approaching 60 wt.%[95,96] or 70 wt.%[25] like in our work. In addition, the Na–S cycling conditions always involve a discharge voltage cut-off lower than 1.0 V in spite of the possible irreversible formation of short-chain Na polysulfides. In addition, the preparation of the sulfur-carbon composite typically includes complex or expensive synthesis steps to achieve the final mixture. Instead, herein we focus on the effect of the electrolyte composition on the reversible Na–S conversion process, which may be heavily affected by the Na polysulfides chemistry occurring at low potential values as suggested in Figure 8. Moreover, our cathode relies on a simple mixture at mild temperatures between carbon black and sulfur with an active material content as high as 70 wt.%, with the aim of studying scalable benchmarks. Therefore, this work proposes a thorough and critical investigation of the complex interplay between the electrolyte and the Na–S chemistry, which is often overlooked.

In this regard, **Figure 9** shows further insights into the morphology of the sulfur cathode and glass-fiber separator upon cycling in Na–S cells achieved by the ex situ SEM analysis. The voltage profiles of the Na–S cells cycled at 35 mA g^{-1} between 1.4 and 2.6 V exploiting either TE-Cl_1% (Figure 9a) or TE-F_1% (Figure 9b) are recorded during the two cycles, performed prior to the morphological study. A specific current as low as 35 mA g^{-1} is selected to allow for an almost full evolution of the electrochemical process, without possible limits typically deriving from polarization. The voltage profiles show for both cells the characteristic evolution of the Na–S conversion process, where the FEC contribution leads to discharge capacities between 1000 and 1300 mAh g^{-1} in the first cycle, while the second one reveals values of ≈600 mAh g^{-1} (Figure 9a,b). After the initial two cycles, the cells are disassembled and the SEM investigations of cathodes and separators are depicted in Figure 9c–j. The cathode cycled with TE-Cl_1% (Figure 9c,d) reveals flat FLG flakes with micrometric size distributed across amorphous particles formed by the active material, conductive carbon, and binder, while the corresponding separator (Figure 9e,f) displays an amorphous precipitate among the glass fibers, possibly due to side reactions from the electrolyte of dissolved polysulfides upon the Na–S conversion. Interestingly, the cathode cycled with TE-F_1% (Figure 9g,h) shows a similar morphology as the one observed for TE-Cl_1%, while remarkable differences can be observed in the SEM micrographs of the separator (Figure 9i,j). The latter exhibits a more extended coverage of the glass fibers than TE-Cl_1% (compared with panels e and f), and shows, in addition, a notable presence of aggregates with micrometric size attributed to the deposition and possible recrystallization of the active material or electrolyte by-products. The above SEM outcomes, which are in line with the photographic images presented in Figure S11 (Supporting Information), confirm that the different chemical environments of the two solutions driven by the conducting salts can actually affect the Na–S electrochemical conversion process. Therefore, the results of this study further highlight the key role of the electrolyte design in achieving advanced configurations of the challenging Na–S system, characterized by a stable electrochemical process and high efficiency.

3. Conclusions

TEGDME-based electrolytes using either $NaClO_4$ (TE-Cl) or $NaCF_3SO_3$ (TE-F) and various concentrations of FEC (i.e., 0.5%, 1%, 2% or 3%) as SEI film-forming agent have been thoroughly analyzed before application in Na–S cells. The bare TE-Cl and

Figure 8. Performance of Na–S cells using either TE-Cl_1% or TE-F_1% with sulfur cathode cast on a FLG-coated current collector. In particular: a,b) CV profiles performed with a) TE-Cl_1% and b) TE-F_1% in the extended 1.0–2.6 V versus Na^+/Na potential range at 0.1 mV s^{-1}; c,d) galvanostatic profiles of cells using c) TE-Cl_1% and d) TE-F_1% cycled at C/20 (1C = 1675 mA g_S^{-1}) between 1.0 and 2.6 V; e–h) galvanostatic cycling performance in terms of e,g) voltage profiles and f,h) corresponding cycling trends (right *y*-axes show coulombic efficiency) of cells using e,f) TE-Cl_1% and g,h) TE-F_1% in the restricted 1.4–2.6 V voltage range at C/20. Panels (f) and (h) also report the cycling trends of the respective Na–S cells in the same operative conditions using the sulfur cathode on bare aluminum (taken from Figures 5 and 6) for better comparison. See Table 1 for electrolyte acronyms.

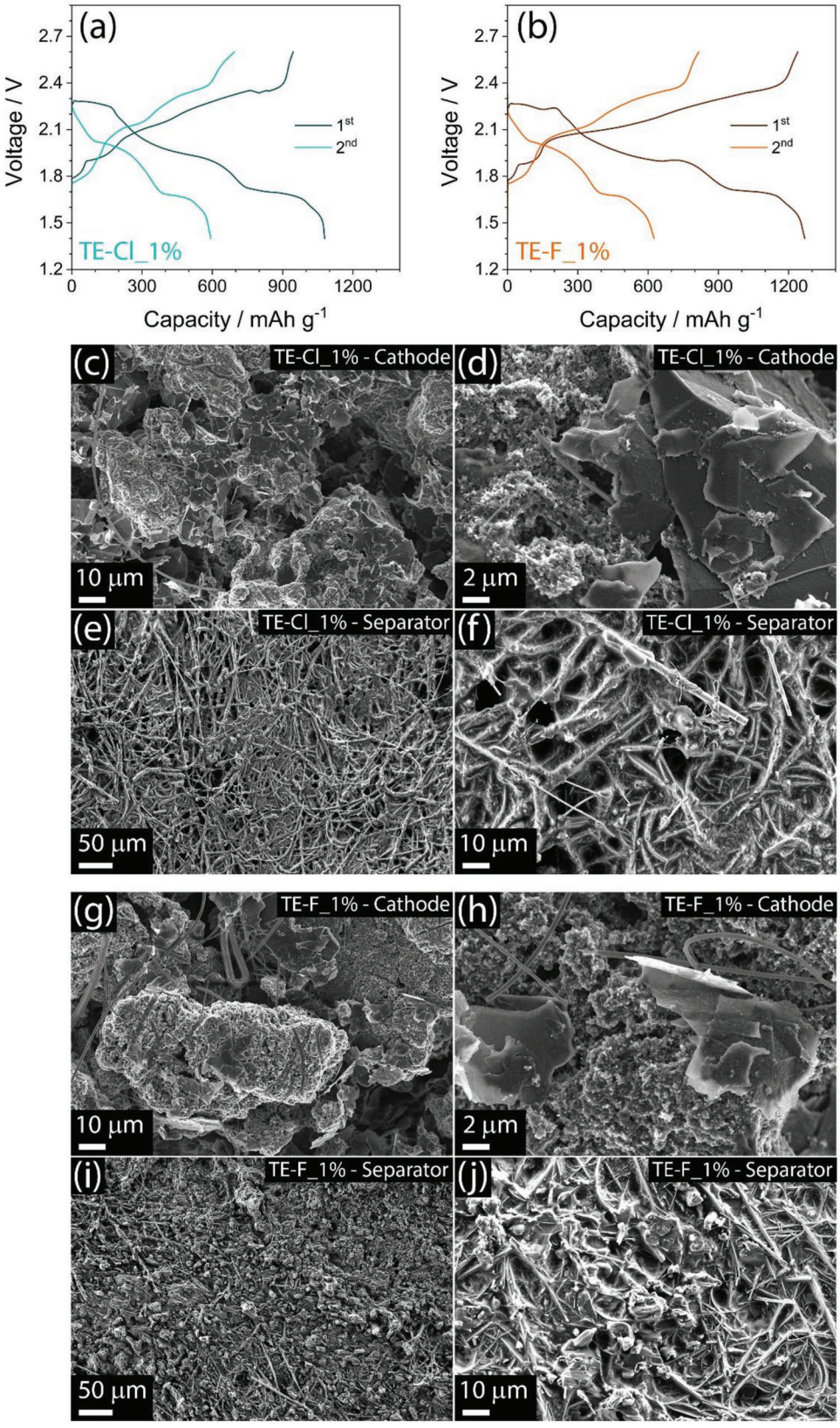

Figure 9. a,b) Voltage profiles related to galvanostatic cycling of Na–S cells carried out at 35 mA g^{-1} employing either a) TE-Cl_1% or b) TE-F_1%; voltage range: 1.4–2.6 V; electrode: S:SPC 70:30 *w/w* on FLG-coated Al support; c–j) ex situ SEM measurements performed on c,d,g,h) sulfur cathode and e,f,i,j) separator retrieved from Na–S cells upon cycling at 35 mA g^{-1} with either (c–f) TE-Cl_1% or (g–j) TE-F_1%. See Table 1 for electrolyte acronyms.

TE-F evidenced thermal stability extending up to 200 °C with the formation of solvent-salt complexes, and similar conductivities approaching 10^{-3} S cm^{-1} at room temperature. Furthermore, TE-Cl showed a t^+ of 0.74 and ESW extended from 0 to 4.52 V versus Na^+/Na, while TE-F revealed a higher t^+ of 0.80 and an ESW limited in the 0–2.98 V versus Na^+/Na range. The data indicated higher Na-stripping/deposition polarization and much more resistive interphase for TE-Cl (≈850 Ω) compared to TE-F (≈2 Ω) upon prolonged aging in Na-cell. The addition of FEC to the bare solutions only slightly influenced the characteristics of the solvated-salt complexes and thermal stability, instead, the Na-cell polarization remarkably changed due to the formation of more resistive and less soluble SEI film using TE-Cl rather than TE-F. Moreover, modifications of the sodium stripping/deposition overvoltage shape suggested possible effects of FEC on the Na electrochemical process kinetics. The FEC addition enhanced the anodic stability to values exceeding 4.5 V versus Na^+/Na for TE-Cl and between 3.8 and 4.1 V versus Na^+/Na for TE-F, and increased the Na-interphase resistance upon aging to values between 840 and 7000 Ω for TE-Cl and from 690 to 3200 Ω for TE-F. The differences have been attributed to the specific chemical nature of the SEI at the Na surface, which is characterized by the predominant presence of reductive decomposition products of the conductive salts, the solvent, and the FEC. In this regard, ex situ SEM performed on Na electrodes upon aging in contact with the electrolytes confirmed the growth of the SEI in concomitance with an increase of the FEC concentration, and notable differences in morphology depending on the composition of the electrolyte solution. The bare electrolytes have been employed in Na–S cells with a benchmark S:SPC 70:30 *w/w* composite cathode cast on Al that showed a conversion process evolving through a double-step discharge at 2.25 and 1.72 V, due to the formation of Na_2S_x ($2 \leq x \leq 8$), reversed in two charge plateaus at 1.95 and 2.32 V with very low efficiency and severe shuttle process, due to the insufficient protection of the Na anode. Instead, the FEC-doped solutions revealed Na–S kinetics influenced by the additive through the promotion of an additional discharge process at ≈1.8 V which greatly enhanced the cell performance. In particular, the cells using TE-Cl_1% and TE-F_1% exhibited long cycle life and coulombic efficiency exceeding 90% and 80%, respectively. Hence, Na–S cells using the bare electrolytes evidenced a weak SEI and poor reaction kinetics, instead TE-Cl_1% and TE-F_1% solutions ensured stable cycling and limited increase of the interphase resistance within a potential range limited between 1.4 and 2.6 V. The Na–S conversion process has been further extended by lowering the reduction potential down to 1.0 V, exploiting a sulfur cathode optimized by an FLG-coated Al collector. However, a modest cycle life and cell failure have been achieved due to the excessive formation of low-chain polysulfides (i.e., Na_2S_2 and Na_2S), and their possible reactivity with the carbon used in the sulfur electrode. On the other hand, the galvanostatic cycling performed within 1.4 and 2.6 V using the optimized cathode with either TE-Cl_1% or TE-F_1% revealed enhanced capacity and coulombic efficiency. Therefore, the data reported in this work evidenced the key importance of the thorough electrolyte investigation for determining the proper setup requested for exploiting advanced Na–S cell configuration.

4. Experimental Section

Electrolytes Preparation: TEGDME ($CH_3(OCH_2CH_2)_4OCH_3$, ≥ 99%, Sigma-Aldrich) was selected as solvent to prepare two electrolytes, one dissolving $NaClO_4$ (ACS reagent, ≥ 98.0%, Sigma-Aldrich) conducting salt with concentration of 1 mol $kg_{solvent}^{-1}$ (1m), and the other dissolving $NaCF_3SO_3$ (98%, Sigma-Aldrich) conducting salt with concentration of 1m. The solutions were indicated in the text as TE-Cl and TE-F, respectively. A set of 8 electrolytes was prepared by adding various concentrations of FEC (≥ 99%, acid < 200 ppm, anhydrous, Sigma-Aldrich) as passivating agents, that was, 0.5%, 1%, 2%, and 3% with respect to the electrolyte weight. The 8 electrolytes were indicated in text as TE-Cl_0.5%, TE-Cl_1%, TE-Cl_2%, TE-Cl_3%, TE-F_0.5%, TE-F_1%, TE-F_2% and TE-F_3%. Table 1 summarizes the acronyms used for the electrolytes and the corresponding compositions. Before use, TEGDME and FEC solvents were stored under molecular sieves (rods, 3 Å, size 1/16 in., Honeywell Fluka) to achieve a water content below 10 ppm as measured by a Karl Fischer 899 Coulometer (Metrohm), while $NaClO_4$ and $NaCF_3SO_3$ were dried under vacuum at 110 °C for two days. All the electrolytes were prepared and stored in an Ar-filled glovebox (MBraun) with H_2O and O_2 levels lower than 1 ppm.

Electrolytes Characterization: TGA of solvents, salts, and electrolytes were performed by temperature scans in the 25-800 °C range under a N_2 flow of 50 mL min^{-1} with a rate of 5 °C min^{-1} via a Mettler-Toledo TGA 2 instrument. Ionic conductivity was evaluated for TE-Cl and TE-F by performing EIS at various temperatures in the 500 kHz–100 Hz frequency range using a 10 mV alternate voltage signal in CR2032 coin-type cells (coin-cells, MTI Corp.) having the stainless-steel|electrolyte|stainless-steel configuration, where the electrolyte was held by an O-ring (23-5FEP-2-50, CS Hyde) with internal diameter of 10 mm, thickness of 127 µm, and cell constant of 0.016 cm^{-1}. The cell temperature was controlled through a Julabo F12 instrument. Symmetrical Na|Na coin-cells employing Na metal electrodes with a diameter of 14 mm separated by a 16 mm-diameter glass-fiber (Whatman GF/B) disc soaked with either TE-Cl or TE-F were prepared to evaluate the Na^+ transference number (t^+) of the two solutions through the Bruce–Vincent–Evans method.[48] The above tests consisted of a chronoamperometric step performed on the cells by applying a voltage of 30 mV (ΔV) for 90 min, alongside EIS measurements carried out before and after polarization in the 500 kHz–100 mHz frequency range using a 10 mV alternate voltage signal. The initial and the steady state currents, as well as the interphase resistance values obtained from the fitting of the EIS spectra (see method below), were used in Equation (1) to calculate t^+:[48]

$$t^+ = \frac{i_{ss}}{i_0} \times \frac{(\Delta V - R_0 i_0)}{(\Delta V - R_{ss} i_{ss})} \quad (1)$$

where i_0 and i_{ss} were the current values at the initial and steady state, respectively, and R_0 and R_{ss} were the interphase resistances before and after cell polarization, respectively. The ESW of the electrolytes was determined by performing voltammetry measurements on coin cells exploiting Na 14 mm-diameter anode and carbon-based cathode separated by a 16 mm-diameter glass-fiber (Whatman GF/B) disc. The carbon-based electrodes were prepared by doctor blade (MTI Corp.) casting on either Al or Cu foil (MTI Corp.) of a slurry composed of SPC (Timcal) at the 80 wt.% and polyvinilidene fluoride (PVDF, Solef 6020) binding agent at the 20 wt.% dispersed in *N*-methyl-2-pyrrolidone (NMP, Sigma-Aldrich). The electrodes were indicated as SPC-Cu and SPC-Al, respectively. The electrode tapes were dried on a hot plate at 70 °C, cut into discs with a 14 mm diameter, and dried under vacuum at 110 °C for 3 h before being transferred in the Ar-filled glovebox. CV measurements were carried out on Na|SPC-Cu cells in the 0.01–2.0 V versus Na^+/Na potential range at a rate of 0.1 mV s^{-1} to evaluate the cathodic stability, while the anodic one was determined by an LSV run performed on Na|SPC-Al cells from the OCV condition to 5 V versus Na^+/Na at 0.1 mV s^{-1}. Sodium stripping/deposition stability was investigated by galvanostatic cycling tests on Na|Na symmetrical cells applying a current of 0.1 mA cm^{-2}: a step time of 1 h was set for both nominal

charge and discharge for coin-cells using 14 mm-diameter Na electrodes separated by two glass-fiber Whatman GF/B 18 mm-discs, while a step time of 10 h was exploited for Swagelok T-type cells using 10 mm Na electrodes separated by three glass-fiber (Whatman GF/B) 10 mm-diameter discs. The stability of the electrolytes upon aging in contact with Na metal was studied via EIS measurements performed in the 500 kHz–100 mHz frequency range through an alternate voltage signal of 10 mV on Na|Na symmetrical coin-cells using 14 mm-diameter Na electrodes separated by a glass-fiber (Whatman GF/B) 16 mm-diameter disc. The EIS tests were carried out every 2 h during the first 14 h after assembling and subsequently every day for 23 days. All the voltammetry and EIS measurements were carried out using a VersaSTAT MC Princeton Applied Research (PAR-AMETEK) instrument, while the galvanostatic cycling data were acquired via a MACCOR 4000 battery test system. All the Nyquist plots recorded by EIS were fitted via NLLS method using the Boukamp software,[45,46] which allowed the description of the spectra with equivalent circuits that include resistive (R) and capacitive (Q) elements. The fitting led to the identification of i) R_e, which was the electrolyte resistance indicated by the high-frequency intercept of the plot; ii) R_i, which defines the electrode/electrolyte interphase resistance measured by the amplitude of the semicircle in the high-medium frequency region including various convoluted contributions, and is arranged in parallel with the Q_i capacitive element in (R_iQ_i); iii) the (R_wQ_w) and Q_w elements, which identify either the finite-length or semi-infinite Warburg-type Na^+ diffusion through either a semicircle or a tilted line, respectively, in the low-frequency region.[45,46] Only fits with a χ^2 of the order of 10^{-4} or lower were accepted.

Fourier transform infrared (FTIR) spectra of the electrolytes were obtained using a Bruker Vertex V70 instrument set up in the transmittance mode.

SEM was performed via a Zeiss Gemini microscope (accelerating voltage of 5 kV) ex situ on Na electrodes retrieved after 1 month of aging from symmetrical Na|Na coin-cells assembled using 10 mm-diameter sodium electrodes and one 16 mm-diameter separator (Whatman GF/B) soaked with the electrolyte. Before SEM measurements, the Na electrodes were washed with 300 µL of diethylene glycol dimethyl ether (DEGDME, anhydrous, 99.5%, Sigma-Aldrich) and subsequently dried under vacuum for 10 min. The DEGDME solvent was dried under molecular sieves (rods, 3 Å, size 1/16 in., Merck) before use.

XPS was performed on Na samples exposed to either TE-Cl, TE-F, TE-Cl_3% or TE-F_3%. Accordingly, Na|Na coin-cells were assembled using 10 mm-diameter sodium electrodes separated by one glass-fiber (Whatman GF/B) 16 mm-diameter disc and aged for 23 days. Subsequently, the cells were disassembled in an Ar-filled glovebox and the Na samples were retrieved, washed with 300 µL of TEGDME, dried under vacuum for 1 h, and transferred to the XPS instrument with a sealed chamber. The XPS measurements were carried out through a Kratos Axis Ultra^{DLD} spectrometer (Kratos Analytical Ltd.) with a monochromated Al K_α X-ray source ($h\nu$ = 1486.6 eV) operating at 20 mA and 15 kV. The wide scans were collected over an analysis area of 300 × 700 µm^2 at a photoelectron pass energy of 160 eV and energy step of 1 eV, while high-resolution spectra were collected at a photoelectron pass energy of 20 eV and an energy step of 0.1 eV. Differential electrical charging effects on the surface of the sample were neutralized during the measurements of all specimens. The spectra were referenced to the adventitious C 1s peak at 284.8 eV. The spectra were analyzed with the CasaXPS software (Casa Software Ltd., version 2.3.24), and the residual background was eliminated by the Shirley method.

Na–S Cells Testing: The sulfur-carbon composite exploited herein was prepared according to previous work.[97] Elemental sulfur (≥ 99.5%, Riedel-de Haën) and SPC were mixed in the 70:30 weight ratio, heated at 125 °C under magnetic stirring with the aid of a silicon oil bath until complete melting of sulfur, cooled at room temperature until solidification of the mixture, and finally ground in an agate mortar to obtain a fine powder. The sulfur-carbon composite was indicated in the text as S:SPC 70:30 *w/w*. The sulfur cathode was prepared by doctor blade casting on aluminum foil (MTI Corp., 15 µm thick) of a slurry composed by 80 wt.% of S:SPC 70:30 *w/w*, 10 wt.% of FLG (produced via WJM method by BeDimensional S.p.A.)[98] as electron conductive agent and structural enhancer,[81] and 10 wt.% of PVDF, dispersed in NMP solvent. The electrode tape was dried at room temperature until complete evaporation of NMP, calendared through an MSK-2150 rolling machine (MTI Corp.) to a final thickness of ≈80 µm, cut into 14 mm-diameter discs and dried under vacuum at 30 °C overnight before being transferred in the Ar-filled glovebox. The final sulfur loading achieved on the cathode surface ranged between 1.7 and 2.0 mg cm^{-2} (electrode geometric area: 1.54 cm^2). CR2032 coin-cells were prepared by stacking a S:SPC 70:30 *w/w* cathode, a 18 mm-diameter glass-fiber separator (Whatman GF/B) soaked with 200 µL of electrolyte, and a 14 mm-diameter sodium anode d(Na–S cells).

CV measurements were carried out on Na–S cells employing TE-Cl, TE-F, TE-Cl_1%, or TE-F_1% between 1.4 and 2.6 V through a scan rate of 0.1 mV s^{-1}. EIS spectra were recorded at the OCV condition of the cell and after 1, 5, and 10 cycles in the 500 kHz–100 mHz frequency range with an alternate voltage signal of 10 mV. The corresponding Nyquist plots were analyzed by NLLS fitting method through Boukamp software as described above, and exclusively accepting results with χ^2 of the order of 10^{-4} or lower.[45,46]

Galvanostatic cycling tests were performed on the Na–S cells by using a constant current rate of C/20 (1C = 1675 mA g^{-1}) in the 1.4–2.6 V voltage range setting a safety step-time of 20 h for charge process in order to switch to discharge if the theoretical capacity (i.e., 1675 mAh g_S^{-1}) was reached.

Additional S:SPC 70:30 *w/w* electrodes were prepared by using an aluminum foil coated with FLG as cathodic support instead of bare aluminum, with final sulfur loading between 1.6 and 2.0 mg cm^{-2} (electrode geometric area: 1.54 cm^2).[81] The FLG-coated Al support was prepared by mixing 90 wt.% of FLG and 10 wt.% of PVDF into NMP solvent, stirring for ≈1 h, doctor-blade casting of the slurry on bare aluminum foil, drying at room temperature until complete evaporation of NMP, and calendared using a MSK-2150 rolling machine to a thickness below 50 µm. The FLG carbon loading on the cathodic support surface was below 2.0 mg cm^{-2}. Na–S cells were prepared using the same configuration described above employing the S:SPC 70:30 *w/w* cathodes on the FLG-coated support and were tested through CV in the 1.0–2.6 V versus Na^+/Na potential range at 0.1 mV s^{-1} and galvanostatic cycling exploiting a rate of C/20 both in the 1.4–2.6 V and 1.0–2.6 V voltage ranges. Additional cycling tests were performed at 35 mA g^{-1} using the S:SPC 70:30 *w/w* cathodes on the FLG-coated support between 1.4and 2.6 V. Upon two discharge/charge cycles, the cells were disassembled in an Ar-filled glovebox to retrieve cathodes and separators, which were washed with TEGDME solvent and dried under vacuum for 1 h. Subsequently, ex situ SEM analyses were carried out on both cathodes and separators using a Zeiss Gemini microscope (accelerating voltage of 5 kV).

The Na–S CV profiles were acquired using a VersaSTAT MC Princeton Applied Research (PAR-AMETEK) instrument, and the galvanostatic cycling tests were carried out via a MACCOR 4000 battery test system setting the room temperature at 30 °C with a maximum fluctuation of ± 0.1 °C.

Acknowledgements

This project was funded under the National Recovery and Resilience Plan (NRRP), Mission 04 Component 2 Investment 1.5- NextGenerationEU, Call for tender n. 3277 dated 30/12/2021, Award Number: 0001052 dated 23/06/2022. The authors also thank the European Union's Horizon 2020 research and innovation program Graphene Flagship under grant agreement No 881603, the grant "Fondo di Ateneo per la Ricerca Scientifica, FAR 2022" University of Ferrara, and the project "Accordo di Collaborazione Quadro 2015" between University of Ferrara (Department of Chemical, Pharmaceutical and Agricultural Sciences) and Sapienza University of Rome (Department of Chemistry). The authors thank the company Be-Dimensional S.p.A., Lungotorrente Secca 30R, Genova, 16163, Italy, for providing the FLG powder used in the electrode composition.

Conflict of Interest

The authors declare no conflict of interest.

Data Availability Statement

The data that support the findings of this study are available from the corresponding author upon reasonable request.

Keywords

FEC, Glyme-electrolytes, $NaCF_3SO_3$, $NaClO_4$, Na–S battery

[1] C. P. Grey, D. S. Hall, *Nat. Commun.* **2020**, *11*, 6279.
[2] D. Di Lecce, R. Verrelli, J. Hassoun, *Green Chem.* **2017**, *19*, 3442.
[3] S. T. Myung, F. Maglia, K. J. Park, C. S. Yoon, P. Lamp, S. J. Kim, Y. K. Sun, *ACS Energy Lett.* **2017**, *2*, 196.
[4] J. Wang, L. Liao, H. R. Lee, F. Shi, W. Huang, J. Zhao, A. Pei, J. Tang, X. Zheng, W. Chen, Y. Cui, *Nano Energy* **2019**, *61*, 404.
[5] G. Calvo, A. Valero, *Environ. Dev* **2022**, *41*, 100640.
[6] A. Valero, A. Valero, G. Calvo, A. Ortego, *Renew. Sustain. Energy Rev.* **2018**, *93*, 178.
[7] D. Kundu, E. Talaie, V. Duffort, L. F. Nazar, *Angew. Chem., Int. Ed.* **2015**, *54*, 3431.
[8] J. Y. Hwang, S. T. Myung, Y. K. Sun, *Chem. Soc. Rev.* **2017**, *46*, 3529.
[9] X. Dou, I. Hasa, D. Saurel, C. Vaalma, L. Wu, D. Buchholz, D. Bresser, S. Komaba, S. Passerini, *Mater. Today* **2019**, *23*, 87.
[10] Z. Yan, L. Zhao, Y. Wang, Z. Zhu, S. Chou, *Adv. Funct. Mater.* **2022**, *32*, 2205622.
[11] Y. Wang, B. Zhang, W. Lai, Y. Xu, S. Chou, H. Liu, S. Dou, *Adv. Energy Mater.* **2017**, *7*, 1602829.
[12] X. Yu, A. Manthiram, *ChemElectroChem* **2014**, *1*, 1275.
[13] C. Ye, Y. Jiao, D. Chao, T. Ling, J. Shan, B. Zhang, Q. Gu, K. Davey, H. Wang, S. Qiao, *Adv. Mater.* **2020**, *32*, 1907557.
[14] S. Xin, Y. X. Yin, Y. G. Guo, L. J. Wan, *Adv. Mater.* **2014**, *26*, 1261.
[15] Q. Guo, S. Sun, K. Kim, H. Zhang, X. Liu, C. Yan, H. Xia, *Carbon Energy* **2021**, *3*, 440.
[16] J. Mou, T. Liu, Y. Li, W. Zhang, M. Li, Y. Xu, J. Huang, M. Liu, *J. Mater. Chem. A* **2020**, *8*, 24590.
[17] W. Lai, H. Wang, L. Zheng, Q. Jiang, Z. Yan, L. Wang, H. Yoshikawa, D. Matsumura, Q. Sun, Y. Wang, Q. Gu, J. Wang, H. Liu, S. Chou, S. Dou, *Angew. Chem. Int. Ed.* **2020**, *59*, 22171.
[18] C. Ye, H. Jin, J. Shan, Y. Jiao, H. Li, Q. Gu, K. Davey, H. Wang, S. Z. Qiao, *Nat. Commun.* **2021**, *12*, 7195.
[19] W. Tang, W. Zhong, Y. Wu, Y. Qi, B. Guo, D. Liu, S. J. Bao, M. Xu, *Chem. Eng. J.* **2020**, *395*, 124978.
[20] D. J. Lee, J. W. Park, I. Hasa, Y. K. Sun, B. Scrosati, J. Hassoun, *J. Mater. Chem. A* **2013**, *1*, 5256.
[21] M. Kohl, F. Borrmann, H. Althues, S. Kaskel, *Adv. Energy Mater.* **2016**, *6*, 1502185.
[22] S. Liu, S. Tang, X. Zhang, A. Wang, Q. H. Yang, J. Luo, *Nano Lett.* **2017**, *17*, 5862.
[23] Z. Huang, S. Wang, X. Guo, J. Safaei, Y. Lei, W. Lai, X. Zhang, B. Sun, D. Shanmukaraj, M. Armand, T. Rojo, G. Wang, *Adv. Mater. Technol.* **2023**, *8*, 2202147.
[24] D. Di Lecce, L. Minnetti, D. Polidoro, V. Marangon, J. Hassoun, *Ionics (Kiel)* **2019**, *25*, 3129.
[25] D. Guo, J. Wang, T. Lai, G. Henkelman, A. Manthiram, *Adv. Mater.* **2023**, *35*, 230084.
[26] Y. X. Ren, H. R. Jiang, T. S. Zhao, L. Zeng, C. Xiong, *J. Power Sources* **2018**, *396*, 304.
[27] S. Wei, S. Xu, A. Agrawral, S. Choudhury, Y. Lu, Z. Tu, L. Ma, L. A. Archer, *Nat. Commun.* **2016**, *7*, 11722.
[28] J. Wu, J. Liu, Z. Lu, K. Lin, Y. Q. Lyu, B. Li, F. Ciucci, J. K. Kim, *Energy Storage Mater.* **2019**, *23*, 8.
[29] J. Ma, M. Wang, H. Zhang, Z. Shang, L. Fu, W. Zhang, B. Song, K. Lu, *Adv. Funct. Mater.* **2023**, *33*, 2214430.
[30] Z. W. Seh, J. Sun, Y. Sun, Y. Cui, *ACS Cent. Sci.* **2015**, *1*, 449.
[31] L. Lutz, D. Alves Dalla Corte, M. Tang, E. Salager, M. Deschamps, A. Grimaud, L. Johnson, P. G. Bruce, J. M. Tarascon, *Chem. Mater.* **2017**, *29*, 6066.
[32] S. Sarkar, M. J. Lefler, B. S. Vishnugopi, R. B. Nuwayhid, C. T. Love, R. Carter, P. P. Mukherjee, *Cell Rep. Phys. Sci.* **2023**, *4*, 101356.
[33] C. Li, H. Xu, L. Ni, B. Qin, Y. Ma, H. Jiang, G. Xu, J. Zhao, G. Cui, *Adv. Energy Mater.* **2023**, *13*, 2301758.
[34] X. Zhang, S. Zhang, J. Lu, F. Tang, K. Dong, Z. Yu, A. Hilger, M. Osenberg, H. Markötter, F. Wilde, S. Zhang, J. Zhao, G. Xu, I. Manke, F. Sun, G. Cui, *Adv. Funct. Mater.* **2024**, 2402253.
[35] B. Qin, Y. Ma, C. Li, H. Xu, J. Li, B. Xie, X. Du, S. Dong, G. Xu, G. Cui, *Energy Storage Mater.* **2023**, *61*, 102891.
[36] H. Xu, C. Li, L. Ni, X. Du, B. Xie, J. Wang, Z. Cui, L. Du, W. Deng, J. Zhao, J. Ju, G. Xu, G. Cui, *Energy Storage Mater.* **2024**, *70*, 103445.
[37] L. Carbone, S. Munoz, M. Gobet, M. Devany, S. Greenbaum, J. Hassoun, *Electrochim. Acta* **2017**, *231*, 223.
[38] A. Ghosh, A. Kumar, A. Roy, M. R. Panda, M. Kar, D. R. MacFarlane, S. Mitra, *ACS Appl. Mater. Interfaces* **2019**, *11*, 14101.
[39] Y. Lee, J. Lee, J. Lee, K. Kim, A. Cha, S. Kang, T. Wi, S. J. Kang, H. W. Lee, N. S. Choi, *ACS Appl. Mater. Interfaces* **2018**, *10*, 15270.
[40] A. Nimkar, N. Shpigel, F. Malchik, S. Bublil, T. Fan, T. R. Penki, M. N. Tsubery, D. Aurbach, *ACS Appl. Mater. Interfaces* **2021**, *13*, 46478.
[41] D. Di Lecce, V. Marangon, H. G. Jung, Y. Tominaga, S. Greenbaum, J. Hassoun, *Green Chem.* **2022**, *24*, 1021.
[42] Y. Ugata, K. Shigenobu, R. Tatara, K. Ueno, M. Watanabe, K. Dokko, *Phys. Chem. Chem. Phys.* **2021**, *23*, 21419.
[43] R. Tatara, Y. Okamoto, Y. Ugata, K. Ueno, M. Watanabe, K. Dokko, *Electrochemistry* **2021**, *89*, 590.
[44] Z. Tian, Y. Zou, G. Liu, Y. Wang, J. Yin, J. Ming, H. N. Alshareef, *Adv. Sci.* **2022**, *9*, 2201207.
[45] B. Boukamp, *Solid State Ion* **1986**, *20*, 31.
[46] B. Boukamp, *Solid State Ion* **1986**, *18–19*, 136.
[47] V. Marangon, Y. Tominaga, J. Hassoun, *J. Power Sources* **2020**, *449*, 227508.
[48] J. Evans, C. A. Vincent, P. G. Bruce, *Polymer (Guildf)* **1987**, *28*, 2324.
[49] D. Morales, R. E. Ruther, J. Nanda, S. Greenbaum, *Electrochim. Acta* **2019**, *304*, 239.
[50] L. G. Chagas, S. Jeong, I. Hasa, S. Passerini, *ACS Appl. Mater. Interfaces* **2019**, *11*, 22278.
[51] D. Di Lecce, D. Campanella, J. Hassoun, *J. Phys. Chem. C* **2018**, *122*, 23925.
[52] Y. Fang, J. Zhang, L. Xiao, X. Ai, Y. Cao, H. Yang, *Adv. Sci.* **2017**, *4*, 1600392.
[53] V. H. Nguyen, M. Le Nguyen, H. P. Tran, V. M. Tran, N. T. Tran, M. L. P. Le, *J. Solid State Electrochem.* **2021**, *25*, 767.
[54] H. Ryu, T. Kim, K. Kim, J. H. Ahn, T. Nam, G. Wang, H. J. Ahn, *J. Power Sources* **2011**, *196*, 5186.
[55] A. Kumar, A. Ghosh, A. Ghosh, A. Ahuja, A. Sengupta, M. Forsyth, D. R. MacFarlane, S. Mitra, *Energy Storage Mater.* **2021**, *42*, 608.
[56] E. Park, J. Park, K. Lee, Y. Zhao, T. Zhou, G. Park, M. G. Jeong, M. Choi, D. J. Yoo, H. G. Jung, A. Coskun, J. W. Choi, *ACS Energy Lett.* **2023**, *8*, 179.

[57] K. Westman, R. Dugas, P. Jankowski, W. Wieczorek, G. Gachot, M. Morcrette, E. Irisarri, A. Ponrouch, M. R. Palacín, J. M. Tarascon, P. Johansson, *ACS Appl. Energy Mater.* **2018**, *1*, 2671.
[58] Y. Liu, R. Jiang, H. Xiang, Z. Huang, Y. Yu, *Electrochim. Acta* **2022**, *425*, 140746.
[59] J. Ma, X. Feng, Y. Wu, Y. Wang, P. Liu, K. Shang, H. Jiang, X. Hou, D. Mitlin, H. Xiang, *J. Energy Chem.* **2023**, *77*, 290.
[60] L. O. Vogt, M. El Kazzi, E. Jämstorp Berg, S. Pérez Villar, P. Novák, C. Villevieille, *Chem. Mater.* **2015**, *27*, 1210.
[61] Q. Ren, Q. Wang, L. Su, G. Liu, Y. Song, X. Shangguan, F. Li, *J. Mater. Chem. A* **2024**, *12*, 1072.
[62] N. C. Su, S. A. M. Noor, M. F. Roslee, N. S. Mohamed, A. Ahmad, M. Z. A. Yahya, *Ionics (Kiel)* **2019**, *25*, 541.
[63] Y. L. Ni'mah, M. Y. Cheng, J. H. Cheng, J. Rick, B. J. Hwang, *J. Power Sources* **2015**, *278*, 375.
[64] V. Marangon, E. Barcaro, E. Scaduti, F. Adami, F. Bonaccorso, V. Pellegrini, J. Hassoun, *ACS Appl. Energy Mater.* **2023**, *6*, 11560.
[65] I. A. Profatilova, C. Stock, A. Schmitz, S. Passerini, M. Winter, *J. Power Sources* **2013**, *222*, 140.
[66] E. Markevich, G. Salitra, M. Afri, Y. Talyosef, D. Aurbach, *J. Electrochem. Soc.* **2020**, *167*, 070509.
[67] H. Kuwata, H. Sonoki, M. Matsui, Y. Matsuda, N. Imanishi, *Electrochemistry* **2016**, *84*, 854.
[68] G. G. Eshetu, T. Diemant, M. Hekmatfar, S. Grugeon, R. J. Behm, S. Laruelle, M. Armand, S. Passerini, *Nano Energy* **2019**, *55*, 327.
[69] D. Di Lecce, V. Marangon, M. Isaacs, R. Palgrave, P. R. Shearing, J. Hassoun, *Small Methods* **2021**, *5*, 2100596.
[70] S. Kim, Y. Jung, J. Park, M. Hong, H. R. Byon, *Bull. Korean Chem. Soc.* **2021**, *42*, 1519.
[71] A. V. Naumkin, A. Kraut-Vass, S. W. Gaarenstroom, C. J. Powell, "NIST X-ray Photoelectron Spectroscopy Database, NIST Standard Reference Database Number 20, National Institute of Standards and Technology, Gaithersburg MD, 20899 (2000)" https://dx.doi.org/10.18434/T4T88K, **2020**.
[72] E. Sahadeo, J. Song, K. Gaskell, N. Kim, G. Rubloff, S. B. Lee, *Phys. Chem. Chem. Phys.* **2018**, *20*, 2517.
[73] S. Kondou, Y. Sakashita, A. Morinaga, Y. Katayama, K. Dokko, M. Watanabe, K. Ueno, *ACS Appl. Mater. Interfaces* **2023**, *15*, 11741.
[74] J. F. Moulder, W. F. Stickle, P. E. Sobol, K. D. Bomben, *Handbook of X-Ray Photoelectron Spectroscopy, Perkin-Elmer Corporation*, Eden Prairie, MN, **1992**.
[75] S. Singsen, S. Suthirakun, P. Hirunsit, P. B. Balbuena, *J. Phys. Chem. C* **2022**, *126*, 16615.
[76] V. Marangon, D. Di Lecce, D. J. L. Brett, P. R. Shearing, J. Hassoun, *J. Energy Chem.* **2022**, *64*, 116.
[77] B. Scrosati, J. Hassoun, Y. K. Sun, *Energy Environ. Sci.* **2011**, *4*, 3287.
[78] H. Zhang, G. G. Eshetu, X. Judez, C. Li, L. M. Rodriguez-Martínez, M. Armand, *Angew. Chem., Int. Ed.* **2018**, *57*, 15002.
[79] A. N. Bhaskarwar, R. Kumar, *Chem. Eng. Sci.* **1986**, *41*, 399.
[80] X. Zhao, Q. Zhu, S. Xu, L. Chen, Z. Zuo, X. Wang, S. Liu, D. Zhang, *J. Electroanal. Chem.* **2019**, *832*, 392.
[81] V. Marangon, E. Barcaro, L. Minnetti, W. Brehm, F. Bonaccorso, V. Pellegrini, J. Hassoun, *Nano Res.* **2023**, *16*, 8433.
[82] J. Wu, Y. Tian, Y. Gao, Z. Gao, Y. Meng, Y. Wang, X. Wang, D. Zhou, F. Kang, B. Li, G. Wang, *Angew. Chem., Int. Ed.* **2022**, *61*, e202205416.
[83] A. Kumar, A. Ghosh, A. Roy, M. R. Panda, M. Forsyth, D. R. MacFarlane, S. Mitra, *Energy Storage Mater.* **2019**, *20*, 196.
[84] E. Zhang, X. Hu, L. Meng, M. Qiu, J. Chen, Y. Liu, G. Liu, Z. Zhuang, X. Zheng, L. Zheng, Y. Wang, W. Tang, Z. Lu, J. Zhang, Z. Wen, D. Wang, Y. Li, *J. Am. Chem. Soc.* **2022**, *144*, 18995.
[85] R. Pai, V. Natu, M. Sokol, M. Carey, T. Greszler, M. W. Barsoum, V. Kalra, *Mater. Today Energy* **2022**, *27*, 101000.
[86] D. Zhao, S. Ge-Zhang, Z. Zhang, H. Tang, Y. Xu, F. Gao, X. Xu, S. Liu, J. Zhou, Z. Wang, Y. Wu, X. Liu, Y. Zhang, *ACS Appl. Mater. Interfaces* **2022**, *14*, 54662.
[87] J. Luo, K. Wang, Y. Qian, P. Wang, H. Yuan, O. Sheng, B. Li, H. Wang, Y. Wang, Y. Liu, J. Nai, X. Tao, W. Li, *Nano Energy* **2023**, *118*, 108958.
[88] Y. Liu, X. Li, Y. Sun, R. Yang, Y. Lee, J. H. Ahn, *J. Alloys Compd.* **2021**, *853*, 157316.
[89] W. Du, K. Shen, Y. Qi, W. Gao, M. Tao, G. Du, S. Bao, M. Chen, Y. Chen, M. Xu, *Nanomicro Lett* **2021**, *13*, 50.
[90] X. Sun, X. Chen, Z. Wang, X. Ai, Y. Cao, J. Zhou, *ACS Appl. Energy Mater.* **2022**, *5*, 11825.
[91] H. Hao, Y. Wang, N. Katyal, G. Yang, H. Dong, P. Liu, S. Hwang, J. Mantha, G. Henkelman, Y. Xu, J. A. Boscoboinik, J. Nanda, D. Mitlin, *Adv. Mater.* **2022**, *34*, 2106572.
[92] F. Xiao, H. Wang, T. Yao, X. Zhao, X. Yang, D. Y. W. Yu, A. L. Rogach, *ACS Appl. Mater. Interfaces* **2021**, *13*, 18010.
[93] X. Ye, S. Luo, Z. Li, J. Ruan, Y. Pang, J. Yang, J. Wang, S. Zheng, *J. Energy Chem.* **2023**, *86*, 620.
[94] Q. Ma, H. Zou, H. He, Y. Li, Z. Fang, *Chem. Eng. J.* **2023**, *474*, 145675.
[95] X. Ye, J. Ruan, Y. Pang, J. Yang, Y. Liu, Y. Huang, S. Zheng, *ACS Nano* **2021**, *15*, 5639.
[96] K. Tang, X. Peng, S. Chen, F. Song, Z. Liu, J. Hu, X. Xie, Z. Wu, *Renew Energy* **2022**, *201*, 832.
[97] D. Di Lecce, V. Marangon, W. Du, D. J. L. Brett, P. R. Shearing, J. Hassoun, *J. Power Sources* **2020**, *472*, 228424.
[98] A. E. Del Rio Castillo, V. Pellegrini, A. Ansaldo, F. Ricciardella, H. Sun, L. Marasco, J. Buha, Z. Dang, L. Gagliani, E. Lago, N. Curreli, S. Gentiluomo, F. Palazon, M. Prato, R. Oropesa-Nuñez, P. S. Toth, E. Mantero, M. Crugliano, A. Gamucci, A. Tomadin, M. Polini, F. Bonaccorso, *Mater. Horiz.* **2018**, *5*, 890.